

DENSE MOLECULAR GAS PROPERTIES OF THE CENTRAL KPC OF NEARBY ULTRALUMINOUS INFRARED GALAXIES CONSTRAINED BY ALMA THREE TRANSITION-LINE OBSERVATIONS

MASATOSHI IMANISHI,^{1, 2, 3} SHUNSUKE BABA,^{4, 1} KOUICHIRO NAKANISHI,^{1, 2} AND TAKUMA IZUMI^{1, 2, 5}

¹*National Astronomical Observatory of Japan, National Institutes of Natural Sciences (NINS), 2-21-1 Osawa, Mitaka, Tokyo 181-8588, Japan*

²*Department of Astronomy, School of Science, Graduate University for Advanced Studies (SOKENDAI), Mitaka, Tokyo 181-8588, Japan*

³*Toyo University, 5-28-20, Hakusan, Bunkyo-ku, Tokyo 112-8606, Japan*

⁴*Kagoshima University, Graduate School of Science and Engineering, Kagoshima 890-0065, Japan*

⁵*Department of Physics, Graduate School of Science, Tokyo Metropolitan University, 1-1 Minami-Osawa, Hachioji-shi, Tokyo 192-0397, Japan*

(Accepted March 9, 2023)

ABSTRACT

We report the results of ALMA 1–2 kpc-resolution, three rotational transition line (J=2–1, J=3–2, and J=4–3) observations of multiple dense molecular gas tracers (HCN, HCO⁺, and HNC) for ten nearby (ultra)luminous infrared galaxies ([U]LIRGs). Following the matching of beam sizes to 1–2 kpc for each (U)LIRG, the high-J to low-J transition-line flux ratios of each molecule and the emission line flux ratios of different molecules at each J transition are derived. We conduct RADEX non-LTE model calculations and find that, under a wide range of gas density and kinetic temperature, the observed HCN-to-HCO⁺ flux ratios in the overall (U)LIRGs are naturally reproduced with enhanced HCN abundance compared to HCO⁺. Thereafter, molecular gas properties are constrained primarily through the use of HCN and HCO⁺ data and the adoption of fiducial values for the HCO⁺ column density and HCN-to-HCO⁺ abundance ratio. We quantitatively confirm the following: (1) Molecular gas at the (U)LIRGs’ nuclei is dense ($\gtrsim 10^{3-4}$ cm⁻³) and warm ($\gtrsim 100$ K). (2) Molecular gas density and temperature in nine ULIRGs’ nuclei are significantly higher than that of one LIRG’s nucleus. (3) Molecular gas in starburst-dominated sources tends to be less dense and cooler than ULIRGs with luminous AGN signatures. For six selected sources, we also apply a Bayesian approach by freeing all parameters and support the above main results. Our ALMA 1–2 kpc resolution, multiple transition-line data of multiple molecules are a very powerful tool for scrutinizing the properties of molecular gas concentrated around luminous energy sources in nearby (U)LIRGs’ nuclei.

1. INTRODUCTION

Galaxies whose infrared (8–1000 μm) luminosities are $L_{\text{IR}} = 10^{12-13}L_{\odot}$ and $L_{\text{IR}} = 10^{11-12}L_{\odot}$ are referred to as ultraluminous infrared galaxies (ULIRGs) and luminous infrared galaxies (LIRGs), respectively (Sanders & Mirabel 1996). Most (U)LIRGs exhibit strong infrared dust thermal radiation which is much brighter than the UV-optical emission, and are found in major mergers of gas-rich galaxies in the nearby universe at $z < 0.3$ (e.g., Sanders & Mirabel 1996). Starburst activity and/or luminous active galactic nucleus (AGN) activity powered by a mass-accreting supermassive black hole (SMBH) at nuclear regions hidden behind the curtain of obscuring gas and dust, are considered the primary energy sources for the observed large infrared luminosities of nearby (U)LIRGs. However, estimating starburst and AGN contribution to the large luminosities is challenging because of very large extinction in nearby (U)LIRGs’ nuclei.

Numerical simulations have predicted that molecular gas is transferred to nuclear regions through merger-induced processes (e.g., Juneau et al. 2009; Moreno et al. 2019) and a large amount of dense ($\gtrsim 10^{3-4} \text{ cm}^{-3}$) molecular gas is observed in nearby merging (U)LIRGs’ nuclei (e.g., Gao & Solomon 2004; Juneau et al. 2009; Imanishi et al. 2019; Ueda et al. 2021; Imanishi et al. 2022). Such dense molecular gas can (1) form stars and become an important fuel toward a central SMBH (i.e., enhancing AGN activity) and (2) be affected by the hidden energy sources of (U)LIRGs, both radiatively and mechanically. Scrutinizing the physical and chemical properties of dense molecular gas at the (U)LIRGs’ nuclei is vital to better understand the nature of these regions. Rotational J-transition emission lines of dense molecular gas tracers are found in the (sub)millimeter wavelength range at 0.3–3.5 mm, where extinction effects are very small. (Sub)millimeter molecular rotational J-transition lines can thus be a very useful tool for the scrutinization.

Spectral line energy distribution (SLED) of CO at (sub)millimeter and far-infrared (30–300 μm), based on large-beam-sized observations with the Herschel Space Observatory and/or ground-based single-dish telescopes ($\gtrsim 5''$ or $\gtrsim 5 \text{ kpc}$ at $z \gtrsim 0.05$), has often been used to identify the presence of luminous AGN activity, in addition to starburst activity, in nearby (U)LIRGs. This is because high-J ($J \gtrsim 4-5$) CO emission can be stronger in an AGN than in a starburst when normalized to low-J ($J = 1-2$) CO luminosity (e.g., Hailey-Dunsheath et al. 2012; Pereira-Santaella et al. 2014; Mashian et al. 2015; Rosenberg et al. 2015; Lu et al. 2017). This can be attributed to the fact that dense and warm ($\gtrsim 100 \text{ K}$) molecular gas in the vicinity of a luminous AGN can excite CO to high-J levels more efficiently than in normal star-forming regions (e.g., Meijerink et al. 2007; Spaans & Meijerink 2008). SLED of molecules with higher dipole moments (e.g., HCN and HCO^+) has also been used to probe the physical conditions of dense molecular gas in nearby (U)LIRGs. However, this has mostly been conducted with large-beam-sized ($\gtrsim 5''$) observations using single dish (sub)millimeter telescopes (e.g., Krips et al. 2008; Greve et al. 2009; Papadopoulos et al. 2014; Israel 2022). Dense molecular gas properties of energetically dominant compact ($\lesssim 1-2 \text{ kpc}$) nuclear regions of nearby ULIRGs (e.g., Soifer et al. 2000; Diaz-Santos et al. 2010; Imanishi et al. 2011; Pereira-Santaella et al. 2021) may not be best probed using these low-angular-resolution data, because emission from spatially extended (\gtrsim a few kpc) host galaxies can be a severe contaminant. Probing only nuclear dense molecular gas through higher-spatial-resolution ($\lesssim 1-2 \text{ kpc}$) observations is highly desirable.

ALMA can facilitate high-angular-resolution ($\lesssim 1''$) and high-sensitivity observations of HCN, HCO^+ and HNC (bright dense molecular gas tracers; Leroy et al. (2017)) at multiple J transitions. Results of $\lesssim 1''$ -resolution HCN, HCO^+ , and HNC observations of nearby (U)LIRGs’

nuclei at J=1–0, J=2–1, J=3–2, and J=4–3 have been reported (e.g., Imanishi & Nakanishi 2013a,b, 2014; Scoville et al. 2015; Aalto et al. 2015a,b; Imanishi et al. 2016b; Martin et al. 2016; Manohar & Scoville 2017; Sliwa & Downes 2017; Imanishi et al. 2018; Saito et al. 2018; Imanishi et al. 2019, 2021; Sakamoto et al. 2021; Imanishi et al. 2022). However, no study has conducted detailed investigations on the physical conditions of nuclear dense molecular gas based on the combination of multiple J-transition line data and non-LTE modeling, except for the nearest ULIRG Arp 220 at $z = 0.018$ (e.g., Tunnard et al. 2015; Sliwa & Downes 2017; Manohar & Scoville 2017). Now that three J-transition line data of HCN, HCO^+ , and HNC are in hand for multiple nearby (U)LIRGs, the time is ripe to do such investigations.

In this paper, we combine available J=2–1, J=3–2, and J=4–3 data¹ of HCN, HCO^+ , and HNC previously obtained from our ALMA observations (Imanishi & Nakanishi 2013a,b, 2014; Imanishi et al. 2016a,b, 2018, 2021, 2022). After matching the beam sizes of all the J-transition line data of all molecules to the same value for each object (1–2 kpc), we perform the aforementioned investigations. Throughout this study, we adopt the cosmological parameters $H_0 = 71 \text{ km s}^{-1} \text{ Mpc}^{-1}$, $\Omega_M = 0.27$, and $\Omega_\Lambda = 0.73$. In addition, molecular line flux ratios are calculated in Jy km s^{-1} . Density and temperature mean H_2 volume number density (n_{H_2}) and kinetic temperature (T_{kin}), respectively, unless otherwise stated.

2. TARGETS

The targets of this study are nine ULIRGs and one LIRG, previously observed at J=2–1, J=3–2, and J=4–3 of HCN, HCO^+ , and HNC, with $\lesssim 1\text{--}2$ kpc resolution, through our ALMA programs (Imanishi & Nakanishi 2013a,b, 2014; Imanishi et al. 2016a,b, 2018, 2021, 2022). Table 1 summarizes the basic properties of the (U)LIRGs. We selected nearby (U)LIRGs with different levels of AGN’s energetic contributions to bolometric luminosity, estimated using optical, infrared, hard X-ray (>10 keV), and (sub)millimeter spectroscopic energy diagnostic methods. Two sources (NGC 1614 and IRAS 13509+0442) and a secondary fainter nucleus of IRAS 12112+0305 (SW) are regarded as starburst-dominated, without discernible luminous AGN signatures, whereas the remaining ULIRGs’ nuclei are diagnosed as containing luminous AGNs. More detailed explanations of the individual (U)LIRGs can be found in Imanishi et al. (2016b). Although the observed ten (U)LIRGs are neither statistically complete nor unbiased, their molecular line studies will provide important information of (1) the general properties of nuclear dense molecular gas in nearby (U)LIRGs at $\lesssim 1\text{--}2$ kpc resolution and (2) possible difference of molecular gas properties between (U)LIRGs’ nuclei with and without luminous AGN signatures.

3. OBSERVATIONS AND DATA ANALYSIS

The details of the majority of HCN, HCO^+ , and HNC line observations have been reported in previous publications (Imanishi & Nakanishi 2013a,b, 2014; Imanishi et al. 2016a,b, 2018, 2021, 2022), and thus are not repeated here. However, the J=4–3 data for HCN, HCO^+ , and HNC for IRAS 06035–7102, and HNC J=4–3 data for IRAS 08572+3915 were not shown in the previous publications. The log of these observations in ALMA Cycle 5 is summarized in Appendix A.

Because different J-transition line data were obtained at different times, with different beam sizes (different array configurations), first, the beam sizes of the multiple J-transition molecular

¹ Redshifted J=1–0 lines for HCN, HCO^+ , and HNC were not observable using ALMA before 2022, in case a source is located at $z \gtrsim 0.06$.

Table 1. Basic Properties of Nine Ultraluminous and One Luminous Infrared Galaxies

Object	Redshift	d _L	Scale	f ₁₂	f ₂₅	f ₆₀	f ₁₀₀	log L _{IR}	Optical	AGN	IR/submm/X
		[Mpc]	[kpc/"]	[Jy]	[Jy]	[Jy]	[Jy]	[L _⊙]	Class	IR [%]	AGN
(1)	(2)	(3)	(4)	(5)	(6)	(7)	(8)	(9)	(10)	(11)	(12)
NGC 1614 ^A	0.0160	68	0.32	1.38	7.50	32.12	34.32	11.7	HII ^{a,b} (Cp ^c)	<5	
IRAS 06035–7102	0.0795	356	1.5	0.12	0.57	5.13	5.65	12.2	LI ^d	22 ⁺³ ₋₁₀	Y ^{h,i,j,k}
IRAS 08572+3915	0.0580	256	1.1	0.32	1.70	7.43	4.59	12.1	LI ^e (Sy2 ^c)	86 ⁺² ₋₃	Y ^{l,m,n,o,p,q,r}
IRAS 12112+0305	0.0730	326	1.4	0.12	0.51	8.50	9.98	12.3	LI ^e (Sy2 ^c)	<0.7	Y ^{s,t} (NE nucleus)
IRAS 12127–1412	0.1332	620	2.3	<0.13	0.24	1.54	1.13	12.2	LI ^e (HII ^c)	88±3	Y ^{h,n,p,r}
IRAS 13509+0442	0.1364	636	2.4	0.10	<0.23	1.56	2.53	12.3	HII ^e (Cp ^c)	<0.03	
IRAS 15250+3609	0.0552	243	1.1	0.16	1.31	7.10	5.93	12.0	LI ^a (Cp ^c)	51 ⁺⁴ ₋₅	Y ^{h,i,r,u}
Superantennae ^B	0.0617	273	1.2	0.22	1.24	5.48	5.79	12.1	Sy2 ^{b,d,f,g}	24±4	Y ^{v,w,x,y}
IRAS 20551–4250	0.0430	188	0.84	0.28	1.91	12.78	9.95	12.0	LI or HII ^d (Cp ^c)	26±3	Y ^{h,z,aa}
IRAS 22491–1808	0.0776	347	1.5	0.05	0.55	5.44	4.45	12.2	HII ^{c,e}	<0.07	Y ^t

^AAlso known as IRAS 04315–0840. This is a LIRG.

^BAlso known as IRAS 19254–7245.

NOTE— Col.(1): Object name. Col.(2): Redshift adopted from ALMA dense molecular line data (Imanishi et al. 2016b). Col.(3): Luminosity distance in Mpc. Col.(4): Physical scale in kpc arcsec⁻¹. Col.(5)–(8): f₁₂, f₂₅, f₆₀, and f₁₀₀ are *IRAS* fluxes at 12 μm, 25 μm, 60 μm, and 100 μm, obtained from Kim & Sanders (1998), Sanders et al. (2003), or the *IRAS* Faint Source Catalog (FSC). Col.(9): Decimal logarithm of infrared (8–1000 μm) luminosity in units of solar luminosity (L_⊙), calculated using $L_{\text{IR}} = 2.1 \times 10^{39} \times D(\text{Mpc})^2 \times (13.48 \times f_{12} + 5.16 \times f_{25} + 2.58 \times f_{60} + f_{100}) \text{ ergs s}^{-1}$ (Sanders & Mirabel 1996). Only NGC 1614 is a LIRG. Col.(10) Optical spectroscopic classification. “Sy2”, “LI”, “HII”, and “Cp” mean Seyfert 2, LINER, HII-region, and starburst+AGN composite, respectively. ^a: Veilleux et al. (1995). ^b: Kewley et al. (2001). ^c: Yuan et al. (2010). ^d: Duc et al. (1997). ^e: Veilleux et al. (1999). ^f: Mirabel et al. (1991). ^g: Colina et al. (1991). Col.(11): Infrared spectroscopically estimated bolometric contribution of AGNs in % by Nardini et al. (2010) for all ULIRGs and by Pereira-Santaella et al. (2015) for the LIRG NGC 1614. Col.(12): Presence (“Y”) of signatures of luminous obscured AGNs, including optically elusive buried ones, in the infrared 3–40 μm and/or hard X-ray (>10 keV) and/or (sub)millimeter spectra, in other representative references: For IRAS 12112+0305 NE and IRAS 22491–1808, certain AGN signatures are found only in the (sub)millimeter range, where the extinction effects are significantly smaller than those in the infrared and X-rays (Hildebrand 1983). ^h: Imanishi et al. (2010). ⁱ: Spoon et al. (2002). ^j: Dartois et al. (2007). ^k: Farrah et al. (2009). ^l: Dudley & Wynn-Williams (1997). ^m: Imanishi & Dudley (2000). ⁿ: Imanishi et al. (2006). ^o: Spoon et al. (2006). ^p: Imanishi et al. (2007). ^q: Armus et al. (2007). ^r: Veilleux et al. (2009). ^s: Imanishi et al. (2016b). ^t: Imanishi et al. (2018). ^u: Stierwalt et al. (2013). ^v: Risaliti et al. (2003). ^w: Imanishi et al. (2008). ^x: Braitto et al. (2009). ^y: Imanishi et al. (2021). ^z: Risaliti et al. (2006). ^{aa}: Sani et al. (2008).

line data were matched with the same value for each object using the CASA task “imsmooth” (THE CASA Team 2022). We adopt 1 kpc if all data were obtained with beam sizes smaller than 1 kpc. This is because (1) the large infrared luminosity of nearby ULIRGs is usually dominated by compact ($\lesssim 1$ –2 kpc) nuclear regions (e.g., Soifer et al. 2000; Diaz-Santos et al. 2010; Imanishi et al. 2011; Pereira-Santaella et al. 2021) and (2) we aim to provide the clearest view of the nuclear dense molecular gas properties of nearby (U)LIRGs by minimizing possible contamination from spatially extended (\gtrsim a few kpc) star-forming regions in the host galaxies. For certain fractions of ULIRGs, certain data exhibit beam sizes larger than 1 kpc. For these cases, the smallest possible beam size (1.5, 1.6, or 2 kpc) is adopted. Table 2 summarizes the beam sizes adopted for individual objects. For IRAS 08572+3915, the beam size of J=4–3 data taken in Cycle 0 is significantly larger than the adopted value (Table 2). However, we assume that a dominant fraction of the observed J=4–3 emission originates from the adopted beam, because of the following reasons. (1) The J=4–3 emission is generally more spatially compact than the lower J-transition lines owing to the higher critical density in the former (Shirley 2015). (2) Changing originally small beam-sized data to unnecessarily large

beam sizes increases the noise in units of mJy beam⁻¹, and thus the scatter of the spectral data becomes large. For J=3–2 data of certain molecular lines for IRAS 12127–1412, IRAS 13509+0442, and the Superantennae, and J=4–3 data for certain lines for IRAS 12112+0305 and IRAS 22491–1808, the major axes of the synthesized beams are slightly larger than the adopted values (Table 2); however, it is also assumed that the bulk of the observed J=3–2 and J=4–3 fluxes are emitted within the adopted beams.

We obtained 1–2 kpc beam spectra by changing the beam size of continuum-subtracted data cube from the original values shown in the previous publications (Imanishi & Nakanishi 2013a,b, 2014; Imanishi et al. 2016a,b, 2018, 2021, 2022), to the adopted ones (Table 2). However, we noticed that the HCN, HCO⁺, and HNC J=4–3 emission lines of IRAS 22491–1808 obtained in ALMA Cycle 0 were substantially narrower than J=3–2 and J=2–1 data obtained in later ALMA Cycles. This is because (1) the molecular-line-derived redshift of $z = 0.0776$ (Imanishi & Nakanishi 2014) was found to be significantly larger than the optically derived redshift of $z = 0.076$ (Kim & Sanders 1998), which had been assumed at the time of the Cycle 0 observation setup, and (2) low-frequency (high-velocity) side of the emission tail was located at the edge of the ALMA spectral windows, which resulted in continuum oversubtraction owing to the improper inclusion of data points with significant emission components. Subsequently, we reanalyzed the HCN, HCO⁺, and HNC J=4–3 Cycle 0 data of IRAS 22491–1808 by redefining a constant continuum flux level. We found that the revised profiles of the J=4–3 emission lines were more consistent with those of the J=2–1 and J=3–2 data, and thus adopt the revised results.

4. RESULTS

Newly obtained spectra of the two ULIRGs, IRAS 06035–7102 and IRAS 08572+3915, which were never presented in our previous publications (Imanishi & Nakanishi 2013a,b, 2014; Imanishi et al. 2016a,b, 2018, 2021, 2022), are shown in Appendix A. Figure 1 displays the velocity profiles for J=2–1, J=3–2, and J=4–3 emission lines of HCN, HCO⁺, and HNC for all the observed (U)LIRGs.

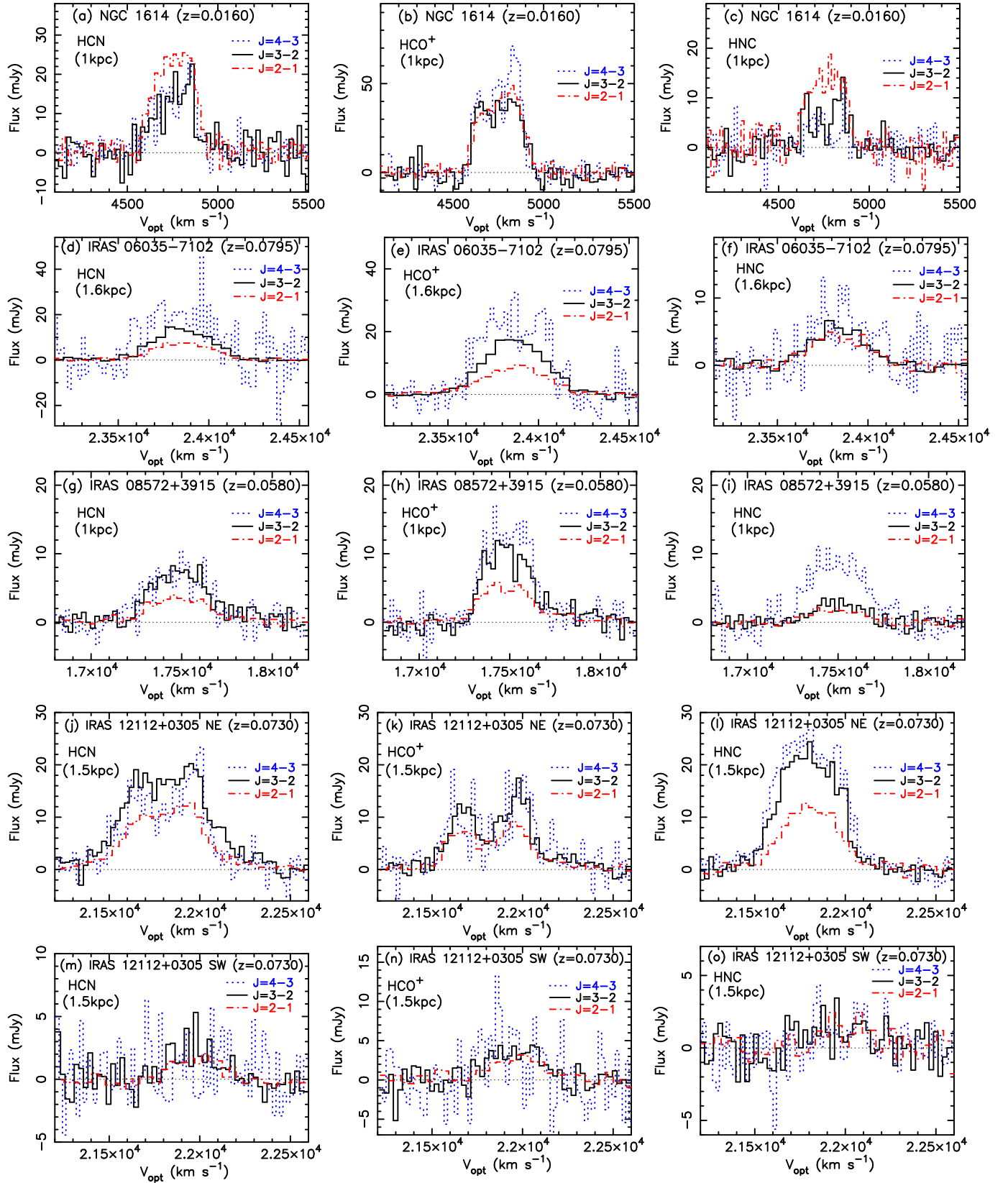
Table 2. Summary of Beam Sizes

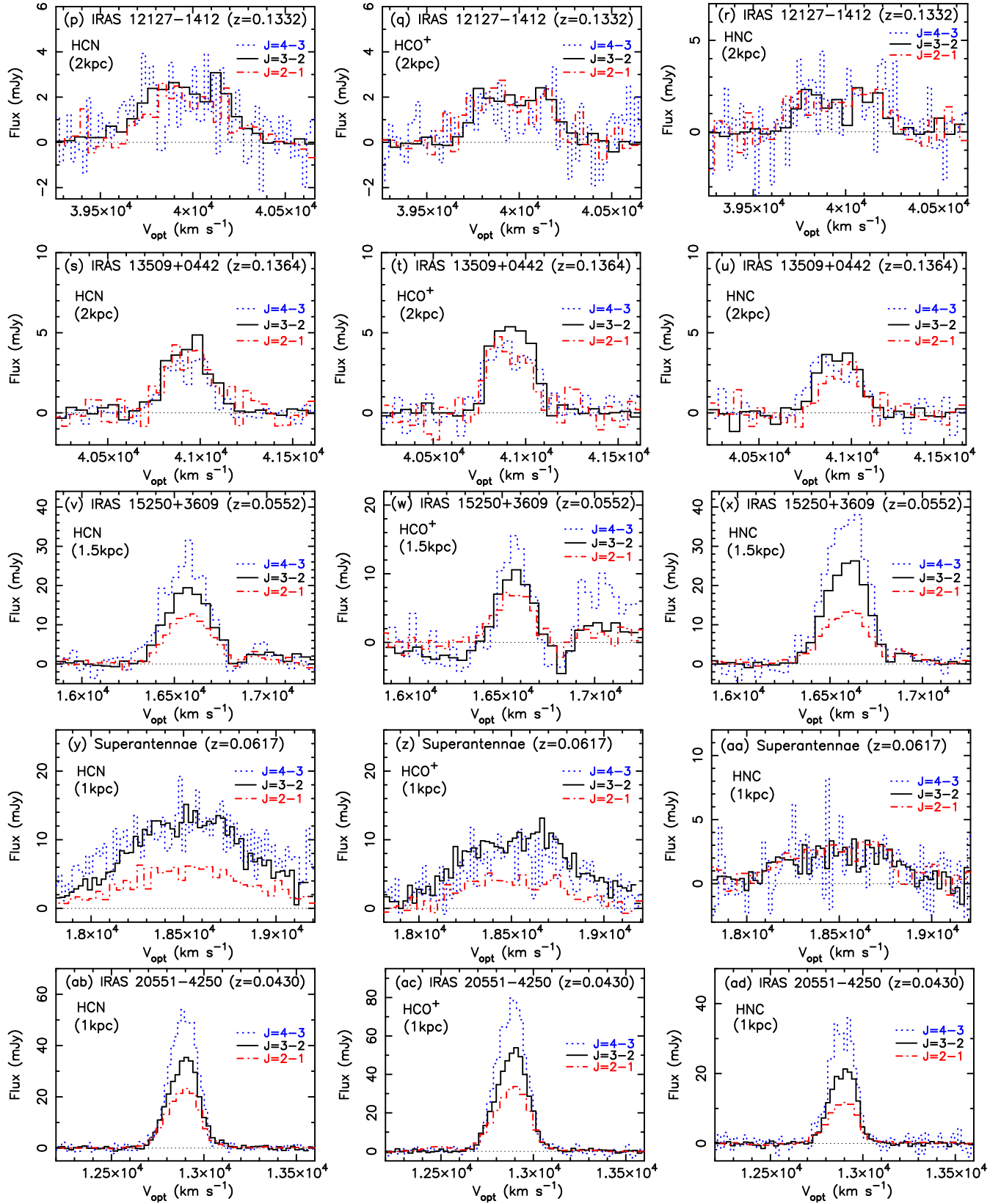
Object	Beam size (arcsec \times arcsec)						Adopted beam arcsec (kpc)
	J21a	J21b	J32a	J32b	J43a	J43b	
(1)	(2)	(3)	(4)	(5)	(6)	(7)	(8)
NGC 1614	0.55 \times 0.37 (Cy5)	0.62 \times 0.35 (Cy5)	1.1 \times 0.58 (Cy2)	1.1 \times 0.39 (Cy2)	1.5 \times 1.3 (Cy0)	1.3 \times 1.3 (Cy0)	3.1'' (1 kpc)
IRAS 06035–7102	1.1 \times 0.80 (Cy5)	0.48 \times 0.34 (Cy5)	1.1 \times 0.78 (Cy3)	1.1 \times 0.74 (Cy3)	0.14 \times 0.16 (Cy5)	0.12 \times 0.09 (Cy5)	1.1'' (1.6 kpc)
IRAS 08572+3915	0.71 \times 0.35 (Cy5)	0.68 \times 0.33 (Cy5)	0.89 \times 0.47 (Cy2)	0.90 \times 0.51 (Cy2)	1.8 \times 1.1 ^A (Cy0)	0.22 \times 0.13 (Cy5)	0.9'' (1 kpc)
IRAS 12112+0305	0.87 \times 0.68 (Cy5)	0.83 \times 0.57 (Cy5)	0.73 \times 0.55 (Cy2)	0.81 \times 0.56 (Cy2)	1.4 \times 0.56 ^B (Cy2)	1.0 \times 0.65 (Cy2)	1.1'' (1.5 kpc)
IRAS 12127–1412	0.29 \times 0.19 (Cy5)	0.24 \times 0.16 (Cy5)	0.94 \times 0.74 ^B (Cy3)	0.86 \times 0.74 (Cy3)	0.60 \times 0.49 (Cy0)	0.61 \times 0.52 (Cy0)	0.86'' (2 kpc)
IRAS 13509+0442	0.27 \times 0.19 (Cy5)	0.29 \times 0.18 (Cy5)	0.99 \times 0.81 ^B (Cy3)	0.92 \times 0.81 ^B (Cy3)	0.70 \times 0.53 (Cy3)	0.69 \times 0.60 (Cy3)	0.84'' (2 kpc)
IRAS 15250+3609	1.1 \times 0.68 (Cy5)	0.70 \times 0.39 (Cy5)	1.2 \times 0.72 (Cy3)	1.3 \times 0.74 (Cy3)	0.87 \times 0.51 (Cy3)	1.1 \times 0.56 (Cy3)	1.4'' (1.5 kpc)
Superantennae	0.54 \times 0.36 (Cy5)	0.49 \times 0.34 (Cy5)	0.87 \times 0.61 ^B (Cy2)	1.0 \times 0.61 ^B (Cy2)	0.74 \times 0.41 (Cy2)	0.61 \times 0.50 (Cy2)	0.85'' (1 kpc)
IRAS 20551–4250	1.1 \times 0.82 (Cy5)	0.60 \times 0.41 (Cy5)	0.50 \times 0.46 (Cy1)	0.52 \times 0.47 (Cy1)	0.55 \times 0.39 (Cy0)	0.64 \times 0.40 (Cy0)	1.2'' (1 kpc)
IRAS 22491–1808	0.50 \times 0.33 (Cy5)	0.41 \times 0.34 (Cy5)	0.92 \times 0.59 (Cy2)	0.41 \times 0.36 (Cy2)	0.56 \times 0.51 (Cy0)	1.1 \times 0.49 ^B (Cy0)	1.0'' (1.5 kpc)

^A Data were obtained in Cycle 0 with a beam size larger than the adopted one. It is assumed that the bulk of the observed J=4–3 flux originates from the nuclear region within the adopted beam (see §3).

^B The major axis is slightly larger than that of the adopted beam. We modify only the minor axis to the adopted value. We assume that the bulk of the observed J=3–2 and J=4–3 flux originates from the nuclear region within the adopted beam (see §3).

NOTE— Col.(1): Object name. Cols.(2)–(7): Beam size of the continuum data in arcsec \times arcsec. Information on the ALMA observing Cycle when individual data were taken, is shown in parentheses. Col.(2): J21a obtained from HCN and HCO⁺ J=2–1 observations. Col.(3): J21b obtained from HNC J=2–1 observations. Col.(4): J32a obtained from HCN and HCO⁺ J=3–2 observations. Col.(5): J32b obtained from HNC J=3–2 observations. Col.(6): J43a obtained from HCN and HCO⁺ J=4–3 observations. Col.(7): J43b obtained from HNC J=4–3 observations. Col.(8) Adopted circular beam size in arcsec. Value in kpc is shown in parentheses.





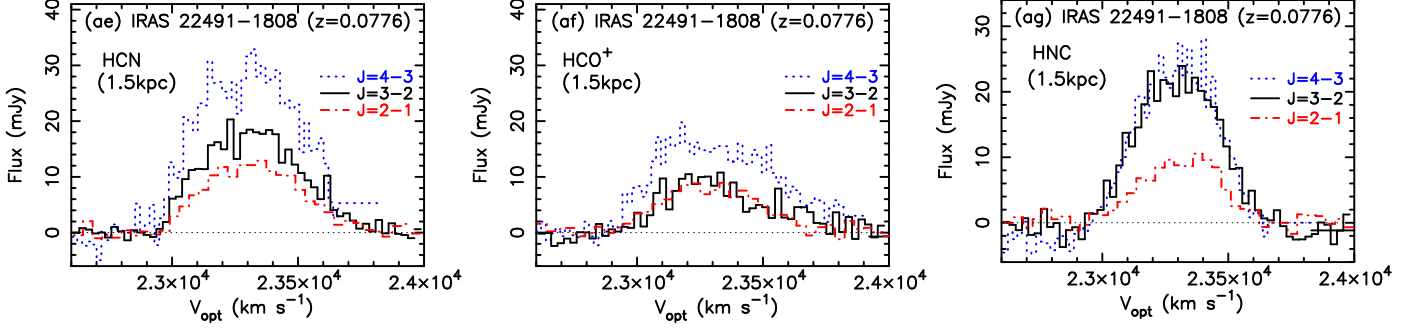


Figure 1. Velocity profiles of emission lines detected for matched beam sizes (1–2 kpc). The abscissa represents the optical local standard of rest (LSR) velocity in km s^{-1} . The ordinate represents the flux density in mJy. (*Left*): HCN. (*Middle*): HCO^+ . (*Right*): HNC. Red dash-dotted line: J=2–1. Black solid line: J=3–2. Blue dotted line: J=4–3. The object name, redshift, and adopted beam size in kpc are shown in each plot. We adopt the rest-frame frequency of $\nu_{\text{rest}} = 177.261$ GHz for HCN J=2–1, $\nu_{\text{rest}} = 265.886$ GHz for HCN J=3–2, $\nu_{\text{rest}} = 354.505$ GHz for HCN J=4–3, $\nu_{\text{rest}} = 178.375$ GHz for HCO^+ J=2–1, $\nu_{\text{rest}} = 267.558$ GHz for HCO^+ J=3–2, $\nu_{\text{rest}} = 356.734$ GHz for HCO^+ J=4–3, $\nu_{\text{rest}} = 181.325$ GHz for HNC J=2–1, $\nu_{\text{rest}} = 271.981$ GHz for HNC J=3–2, and $\nu_{\text{rest}} = 362.630$ GHz for HNC J=4–3. The horizontal black thin dotted straight line indicates the zero flux level.

Gaussian fits are applied to estimate the emission line fluxes within the adopted beam sizes. Single Gaussian fits are adopted, except for the HCN and HCO^+ lines of IRAS 12112+0305 NE, which clearly exhibit a double-peaked profile with a strong central dip (Figure 1j,k) wherein the results of a double Gaussian fit are adopted. For certain emission lines from other sources, certain weak signatures of double-peaked profiles with modest amounts of central dips are observed; however, we decide to adopt single Gaussian fitting results after confirming that the flux estimates between the single and double Gaussian fits agree within $\sim 10\%$ for significantly detected emission lines ($\gtrsim 3\sigma$). This is because we aim to estimate the fluxes of multiple J-transition emission lines in a consistent manner, using the simplest profile possible. The final Gaussian fitting results are summarized in Appendix B.

The flux density of the continuum emission, simultaneously taken during individual molecular line observations, is also estimated using the adopted beam sizes for individual (U)LIRGs. Flux density and spectral energy distribution (SED) of the continuum emission are summarized in Appendix C.

Table 3 summarizes the adopted Gaussian-fit velocity-integrated emission line fluxes of HCN, HCO^+ , and HNC at J=2–1, J=3–2, and J=4–3, together with the adopted line width which will be used for model calculations in §5. Table 4 and Figure 2a show the derived HCN-to- HCO^+ flux ratios at J=2–1, J=3–2, and J=4–3. High-J to low-J emission line flux ratios for HCN, HCO^+ , and HNC are summarized in Table 5, and those for the HCN and HCO^+ are plotted in Figure 2b.

The high-J to low-J (J=2–1) flux ratios of the LIRG NGC 1614 are smaller than those of the remaining ULIRGs particularly for HCN (by a factor of 2–5 except IRAS 13509+0442) and for HCO^+ as well (by a factor of 1–3) (Figure 2b and Table 5), suggesting that gas density and temperature of NGC 1614 are much lower and thus collisional excitation to high-J levels (J=3 and 4) is insufficient. Furthermore, only NGC 1614 shows (1) a clear systematic decreasing trend in the HCN-to- HCO^+ flux ratio from low-J to high-J transition in Figure 2a and (2) significantly smaller high-J to low-J flux ratios for HCN than for HCO^+ in Figure 2b, while the remaining ten ULIRGs’ nuclei do not except IRAS 13509+0442 which shows a weaker, but similar decreasing trend in the former. These

Table 3. Adopted Nuclear Dense Molecular Line Flux and Width

Object	HCN			HCO ⁺			HNC			Δv
	J=2-1	J=3-2	J=4-3	J=2-1	J=3-2	J=4-3	J=2-1	J=3-2	J=4-3	
	[Jy km s ⁻¹]			[Jy km s ⁻¹]			[Jy km s ⁻¹]			
(1)	(2)	(3)	(4)	(5)	(6)	(7)	(8)	(9)	(10)	(11)
NGC 1614	6.8±0.4	4.2±0.8	4.3±0.5	12±1	11±1	14±1	3.7±0.4	2.0±0.6	1.1±0.6	250
IRAS 06035−7102	2.9±0.1	5.1±0.2	8.8±1.8	3.6±0.1	6.8±0.2	10±1	1.6±0.1	1.9±0.2	2.6±0.6	350
IRAS 08572+3915	1.4±0.1	2.8±0.2	2.8±0.3	1.8±0.1	3.3±0.3	4.2±0.3	0.61±0.09	0.84±0.13	3.3±0.3	300
IRAS 12112+0305 NE	5.5±1.0	9.4±1.2	7.2±1.7	3.4±0.3	5.0±0.4	5.5±1.2	4.3±0.2	8.6±0.3	11±1	350
IRAS 12112+0305 SW	0.49±0.10	0.76±0.23	<1.0 ^A	0.96±0.16	1.2±0.3	1.4±0.7	0.44±0.17	0.62±0.30	0.49±0.19	300
IRAS 12127−1412	0.94±0.21	1.3±0.1	1.2±0.2	0.95±0.23	0.97±0.09	0.81±0.30	0.93±0.20	0.84±0.15	1.0±0.3	500
IRAS 13509+0442	1.0±0.2	1.1±0.1	0.83±0.11	1.0±0.2	1.4±0.1	1.2±0.2	0.57±0.14	0.91±0.07	0.84±0.13	250
IRAS 15250+3609	3.5±0.2	5.5±0.3	7.5±0.5	1.7±0.2	2.0±0.3	2.5±0.7	4.1±0.3	7.1±0.3	10±1	250
Superantennae	4.9±0.4	11±1	14±1	2.9±0.3	8.2±0.3	6.1±0.6	1.9±0.2	1.7±0.2	1.7±0.5	800
IRAS 20551−4250	4.8±0.1	6.8±0.1	9.6±0.2	7.4±0.1	11±1	15±1	2.3±0.1	3.7±0.1	5.6±0.2	200
IRAS 22491−1808	5.5±0.2	8.4±0.3	14±1	3.8±0.2	4.2±0.4	9.4±0.5	3.6±0.3	8.6±0.4	9.2±0.5	400

^AThis 3 σ upper limit is estimated from a 1.5 kpc beam moment 0 map.

NOTE— Col.(1): Object name. Cols.(2)–(10): Adopted Gaussian-fit velocity-integrated flux of the dense molecular emission line in Jy km s⁻¹ used in our discussion (§5). Only the statistical uncertainty of the Gaussian fit is included. Col.(2): HCN J=2–1. Col.(3): HCN J=3–2. Col.(4): HCN J=4–3. Col.(5): HCO⁺ J=2–1. Col.(6): HCO⁺ J=3–2. Col.(7): HCO⁺ J=4–3. Col.(8): HNC J=2–1. Col.(9): HNC J=3–2. Col.(10): HNC J=4–3. Col.(11): Adopted line width in km s⁻¹ based on our Gaussian fit (FWHM value in Table 9, column 6). This line width will be used for our RADEX non-LTE model calculations.

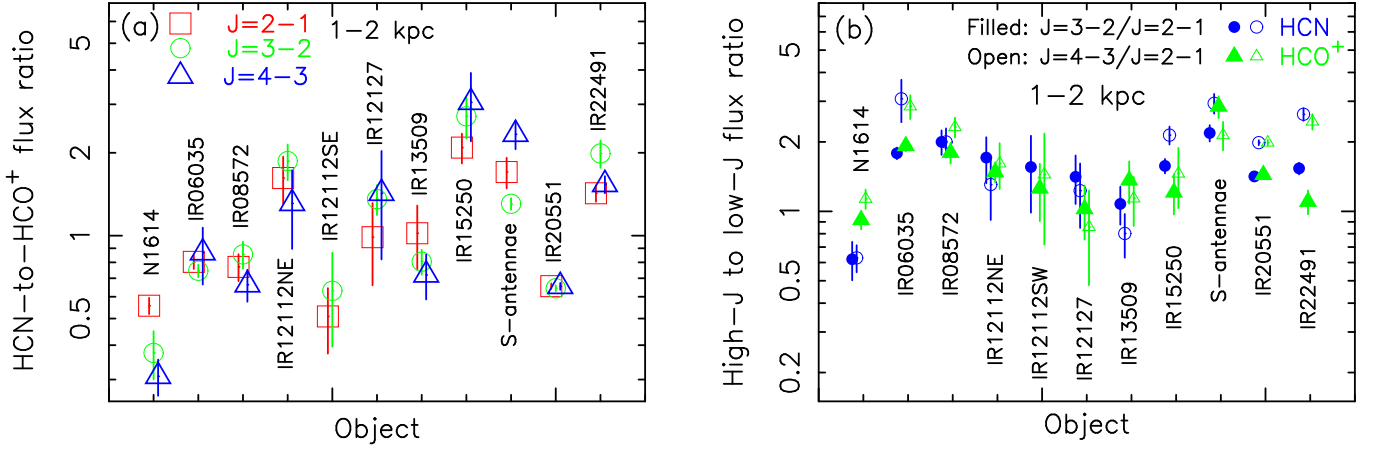


Figure 2. (a): HCN-to-HCO⁺ flux ratio (ordinate) with a 1–2 kpc beam size at J=2–1 (red open square), J=3–2 (green open circle), and J=4–3 (blue open triangle). J=4–3 data of IRAS 12112+0305 SW are not shown because no HCN J=4–3 emission line is detected. (b): J=3–2 to J=2–1 (filled) and J=4–3 to J=2–1 (open) flux ratio of HCN (blue circle) to HCO⁺ (green triangle), calculated from 1–2 kpc beam-sized flux measurements of individual lines in Jy km s⁻¹. For IRAS 12112+0305 SW, the flux ratio of HCN J=4–3 to J=2–1 is not shown, because the HCN J=4–3 emission line is not detected.

Table 4. HCN-to-HCO⁺ Flux Ratio

Object	$\frac{\text{HCN}}{\text{HCO}^+}$ J=2–1	$\frac{\text{HCN}}{\text{HCO}^+}$ J=3–2	$\frac{\text{HCN}}{\text{HCO}^+}$ J=4–3
(1)	(2)	(3)	(4)
NGC 1614 (1 kpc)	0.56±0.04	0.38±0.07	0.31±0.05
IRAS 06035–7102 (1.6 kpc)	0.80±0.05	0.75±0.04	0.87±0.20
IRAS 08572+3915 (1 kpc)	0.77±0.09	0.85±0.10	0.66±0.09
IRAS 12112+0305 NE (1.5 kpc)	1.6±0.3	1.9±0.3	1.3±0.4
IRAS 12112+0305 SW (1.5 kpc)	0.51±0.14	0.63±0.24	<1.3
IRAS 12127–1412 (2 kpc)	0.99±0.33	1.4±0.2	1.4±0.6
IRAS 13509+0442 (2 kpc)	1.0±0.3	0.80±0.08	0.72±0.13
IRAS 15250+3609 (1.5 kpc)	2.1±0.3	2.7±0.5	3.1±0.9
Superantennae (1 kpc)	1.7±0.2	1.3±0.1	2.3±0.3
IRAS 20551–4250 (1 kpc)	0.66±0.01	0.64±0.02	0.65±0.02
IRAS 22491–1808 (1.5 kpc)	1.4±0.1	2.0±0.2	1.5±0.1

NOTE— Col.(1): Object name. The adopted beam size in kpc is shown in parentheses. Cols.(2)–(4): The HCN-to-HCO⁺ emission line flux ratio calculated in units of Jy km s^{−1}. Col.(2): J=2–1. Col.(3): J=3–2. Col.(4): J=4–3. Only the Gaussian-fit statistical uncertainty is considered because both HCN and HCO⁺ data at each J-transition were obtained simultaneously, and so their flux ratio is not affected by the possible absolute flux calibration uncertainty of individual ALMA observations.

Table 5. High-J to Low-J Molecular Emission Line Flux Ratio

Object	HCN			HCO ⁺			HNC		
	$\frac{J=3-2}{J=2-1}$	$\frac{J=4-3}{J=2-1}$	$\frac{J=4-3}{J=3-2}$	$\frac{J=3-2}{J=2-1}$	$\frac{J=4-3}{J=2-1}$	$\frac{J=4-3}{J=3-2}$	$\frac{J=3-2}{J=2-1}$	$\frac{J=4-3}{J=2-1}$	$\frac{J=4-3}{J=3-2}$
(1)	(2)	(3)	(4)	(5)	(6)	(7)	(8)	(9)	(10)
NGC 1614 (1 kpc)	0.62±0.12	0.63±0.08	1.0±0.2	0.92±0.08	1.1±0.1	1.2±0.1	0.54±0.16	0.30±0.18	0.55±0.35
IRAS 06035–7102 (1.6 kpc)	1.8±0.1	3.1±0.6	1.7±0.4	1.9±0.1	2.9±0.3	1.5±0.2	1.2±0.1	1.6±0.4	1.4±0.4
IRAS 08572+3915 (1 kpc)	2.0±0.2	2.0±0.3	1.0±0.1	1.8±0.2	2.3±0.2	1.3±0.1	1.4±0.3	5.5±1.0	4.0±0.7
IRAS 12112+0305 NE (1.5 kpc)	1.7±0.4	1.3±0.4	0.76±0.21	1.5±0.1	1.6±0.4	1.1±0.2	2.0±0.1	2.4±0.2	1.2±0.1
IRAS 12112+0305 SW (1.5 kpc)	1.6±0.6	<2.4	<1.8	1.3±0.4	1.4±0.7	1.1±0.6	1.4±0.9	1.1±0.6	0.79±0.49
IRAS 12127–1412 (2 kpc)	1.4±0.3	1.2±0.4	0.87±0.20	1.0±0.3	0.86±0.38	0.84±0.32	0.91±0.25	1.1±0.4	1.2±0.4
IRAS 13509+0442 (2 kpc)	1.1±0.2	0.80±0.17	0.74±0.10	1.4±0.3	1.1±0.3	0.83±0.13	1.6±0.4	1.5±0.4	0.93±0.16
IRAS 15250+3609 (1.5 kpc)	1.6±0.1	2.1±0.2	1.4±0.1	1.2±0.2	1.5±0.4	1.2±0.4	1.8±0.2	2.5±0.2	1.4±0.1
Superantennae (1 kpc)	2.2±0.2	2.9±0.3	1.3±0.1	2.8±0.3	2.1±0.3	0.75±0.08	0.89±0.14	0.89±0.25	1.0±0.3
IRAS 20551–4250 (1 kpc)	1.4±0.1	2.0±0.1	1.4±0.1	1.4±0.1	2.0±0.1	1.4±0.1	1.6±0.1	2.5±0.1	1.5±0.1
IRAS 22491–1808 (1.5 kpc)	1.5±0.1	2.6±0.2	1.7±0.1	1.1±0.1	2.5±0.2	2.2±0.3	2.4±0.2	2.6±0.3	1.1±0.1

NOTE—Col.(1): Object name. The adopted beam size in kpc is shown in parentheses. Cols.(2)–(10): High-J to low-J flux ratio of dense molecular emission line measured in Jy km s^{−1}. Only the statistical uncertainty of the Gaussian fit is considered. Col.(2): HCN J=3–2 to J=2–1. Col.(3): HCN J=4–3 to J=2–1. Col.(4): HCN J=4–3 to J=3–2. Col.(5): HCO⁺ J=3–2 to J=2–1. Col.(6): HCO⁺ J=4–3 to J=2–1. Col.(7): HCO⁺ J=4–3 to J=3–2. Col.(8): HNC J=3–2 to J=2–1. Col.(9): HNC J=4–3 to J=2–1. Col.(10): HNC J=4–3 to J=3–2.

results can also be explained by the lower gas density and temperature in NGC 1614 because the critical density of HCN is a factor of ~ 5 higher than that of HCO^+ (Shirley 2015); thus, collisional excitation to a high J-level is less efficient for HCN than for HCO^+ in low-density and low-temperature molecular gas. We will employ non-LTE model calculations to quantitatively constrain the nuclear dense molecular gas properties of the LIRG NGC 1614 and the remaining ULIRGs in more detail in the next section (§5).

5. DISCUSSION

5.1. General Descriptions of Our RADEX Non-LTE Modeling

There are now three rotational transition line data (J=2–1, J=3–2, and J=4–3) of HCN, HCO^+ , and HNC, whose fluxes are measured with the same beam sizes (1–2 kpc) for individual (U)LIRGs. To investigate nuclear (1–2 kpc) molecular gas properties in detail, the observed emission line flux ratios are compared with the calculated flux ratios using RADEX (van der Tak et al. 2007). RADEX is a non-LTE radiative transfer code that solves the statistical equilibrium problems in a one-zone medium based on the escape probability approximations. Molecular emission line flux ratios in the RADEX code are primarily determined by the following three parameters: (i) H_2 volume number density (n_{H_2}). (ii) H_2 kinetic temperature (T_{kin}). (iii) Molecular column density divided by line width ($N_{\text{mol}}/\Delta v$), which reflects the line opacity, where Δv can be derived from the observed molecular line width (Table 3, column 11). We constrain these three parameters from the three J-transition line data.

In all RADEX non-LTE calculations, molecular gas is assumed to be static and spherically symmetric homogeneous medium. The background temperature is set as the cosmic microwave background (2.73 K). The collision partner for HCN, HCO^+ , and HNC is regarded as H_2 only. The emission line flux ratios are calculated after converting the fluxes from Kelvin (brightness temperature) to Jy units, as adopted in Tables 4–5. For implementation, `pyradex`², a Python wrapper for RADEX, is used.

To perform the RADEX non-LTE calculations, we use only the HCN and HCO^+ data, but exclude the HNC data for the following two reasons. First, in previous observations of the Galactic sources, the HNC abundance is found to be very low in warm molecular gas in the vicinity of a luminous energy source (e.g., Schilke et al. 1992; Hirota et al. 1998; Graninger et al. 2014; Bublitz et al. 2019). In fact, in the nearby ($z = 0.0038$, luminosity distance ~ 14 Mpc), well-studied AGN NGC 1068, the HNC emission is found to be extremely weak, compared with HCN and HCO^+ , in close proximity to the central luminous AGN (Imanishi et al. 2020). Therefore, HNC is not considered to be as good as HCN and HCO^+ to investigate the physical properties of warm molecular gas near luminous energy sources (AGN and/or starburst) at the center of (U)LIRGs’ nuclei. Second, the HNC data were not taken simultaneously with the HCN and HCO^+ data at the same J-transition (Imanishi & Nakanishi 2013a,b, 2014; Imanishi et al. 2016a,b, 2018, 2021, 2022). Thus, possible absolute flux calibration uncertainty of three more ALMA observations (HNC J=2–1, J=3–2, and J=4–3) must be considered as additional free parameters for our RADEX non-LTE calculations (see §5.3 and 5.5), which makes

² <https://github.com/keflavich/pyradex>

it extremely difficult to find the best fit values without systematic uncertainty under the limited number of observational constraints.

5.2. *HCN-to-HCO⁺ Emission Line Flux Ratios*

In the RADEX model calculations for the (U)LIRGs’ nuclei, we set density and temperature in the range 10^3 – 10^8 cm^{−3} and 10–1000 K, respectively. We also adopt the HCO⁺ column density with $N_{\text{HCO}^+} = 1 \times 10^{16}$ cm^{−2} as the fiducial value, by assuming that the observed (U)LIRGs are modestly Compton-thick ($N_{\text{H}} \sim \text{a few} \times 10^{24}$ cm^{−2}) and the HCO⁺-to-H₂ abundance ratio is $\sim 10^{-8}$ (e.g., Martin et al. 2006; Saito et al. 2018).

Figure 3 shows a three-dimensional plot of the HCN-to-HCO⁺ emission line flux ratio at J=2–1, J=3–2, and J=4–3. The overall distribution of the observed HCN-to-HCO⁺ flux ratios for the (U)LIRGs’ nuclei can be naturally reproduced with the HCN-to-HCO⁺ abundance ratio of $[\text{HCN}]/[\text{HCO}^+] = 3$ rather than 1. In Appendix D, we also make the same plot with $[\text{HCN}]/[\text{HCO}^+] = 7$ and 1, and confirm that the enhanced HCN-to-HCO⁺ abundance ratio can better fit the observed flux ratios for the majority of the (U)LIRGs’ nuclei. Two sources with small HCN-to-HCO⁺ flux ratios, located at the bottom-left part of Figure 3 (NGC 1614 and IRAS 12112+0305 SW) may be better reproduced with $[\text{HCN}]/[\text{HCO}^+] = 1$ (i.e., comparable HCN and HCO⁺ abundances). Both of these sources are classified as starburst-dominated (§2). However, the remaining ULIRGs showing luminous AGN signatures (except IRAS 13509+0442) are better reproduced with enhanced HCN abundance relative to HCO⁺. In fact, the enhanced HCN-to-HCO⁺ abundance ratio (1) has been reported in dense molecular gas around luminous AGNs (e.g., Krips et al. 2008; Aladro et al. 2015; Saito et al. 2018; Nakajima et al. 2018; Takano et al. 2019; Kamenno et al. 2020; Imanishi et al. 2020; Butterworth et al. 2022), and (2) has been argued to be necessary to reproduce the HCN-to-HCO⁺ flux ratios with larger than unity, as observed in many (U)LIRGs (e.g., Yamada et al. 2007; Izumi et al. 2016a). We adopt this enhanced HCN abundance of $[\text{HCN}]/[\text{HCO}^+] = 3$ as the fiducial value for our model calculations in the next subsection. As we will show in the calculations for the starburst-dominated LIRG NGC 1614 (Figure 4), adopting $[\text{HCN}]/[\text{HCO}^+] = 1$ provides comparable gas density and temperature³.

We also perform calculations using the HCO⁺ column density of $N_{\text{HCO}^+} = 1 \times 10^{15}$ cm^{−2} (an order of magnitude smaller than that adopted in Figure 3) and a line width of $\Delta v = 800$ km s^{−1} (a factor of >2 broader). However, the overall trend of the RADEX-calculated HCN-to-HCO⁺ flux ratios does not change significantly (Appendix D).

5.3. *High-J to Low-J Emission Line Flux Ratios*

To quantitatively estimate the density and temperature of molecular gas at (U)LIRGs’ nuclei, a total of four observed line flux ratios, J=3–2 to J=2–1 and J=4–3 to J=2–1 of HCN and HCO⁺ (Table 5) are fitted using the RADEX model. Least-squares fitting of $\log n_{\text{H}_2}$ (density) and $\log T_{\text{kin}}$ (temperature) is performed using conventional Levenberg-Marquardt algorithm through Python package `lmfit` (Newville et al. 2021). The confidence intervals for the parameters are examined by grid computing $\Delta\chi^2 \equiv \chi^2 - \chi_{\text{best}}^2$ with $\log n_{\text{H}_2}$ ranging from 2–6 and $\log T_{\text{kin}}$ from 1–3. Figure 4a shows the derivation of molecular gas density and temperature that can best reproduce the observed J=3–2 to J=2–1 and J=4–3 to J=2–1 flux ratios of HCN and HCO⁺ for the starburst-dominated

³ Our main argument about gas density and temperature at (U)LIRGs’ nuclei (§5.3–5.4) also will not change even calculating with $[\text{HCN}]/[\text{HCO}^+] = 7$.

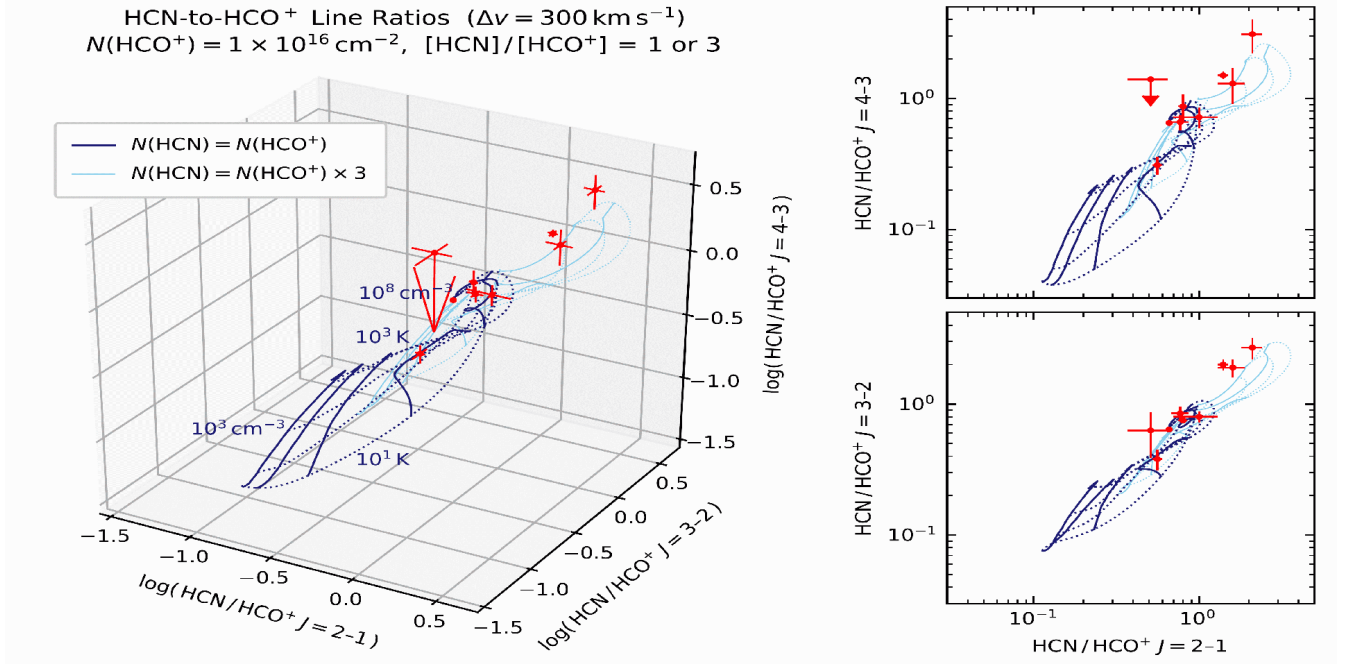


Figure 3. Comparison of the observed and RADEX-calculated HCN-to-HCO⁺ flux ratios. (*Left panel*): 3D plot of HCN-to-HCO⁺ flux ratios at J=2-1, J=3-2, and J=4-3. The red points indicate the observed values. Only nine (U)LIRGs’ nuclei with adopted line widths $\Delta v = 200-400 \text{ km s}^{-1}$ (excluding IRAS 12127-1412 and the Superantennae) (Table 3) are included here. The overlaid blue meshes show the RADEX-calculated results computed over the range of density $\log(n_{\text{H}_2}/\text{cm}^{-3}) = 3-8$ in steps of 0.1 and temperature $\log(T_{\text{kin}}/\text{K}) = 1-3$ in steps of 0.05. The solid lines represent the iso-density results ($\log n_{\text{H}_2} = 3, 4, 5, 6, 7, 8$), whereas the dotted lines represent the iso-temperature results ($\log T_{\text{kin}} = 1.0, 1.5, 2.0, 2.5, 3.0$). In the calculations, the line width and HCO⁺ column density are fixed at $\Delta v = 300 \text{ km s}^{-1}$ and $N_{\text{HCO}^+} = 1 \times 10^{16} \text{ cm}^{-2}$, respectively. The results of HCN-to-HCO⁺ abundance ratio of $[\text{HCN}]/[\text{HCO}^+] = 1$ or 3 are shown in dark and light blue colors, respectively. (*Right panels*): Projection of the 3D plot along J=3-2 (*upper*) and J=4-3 (*lower*) directions.

LIRG NGC 1614, by adopting fiducial values of $N_{\text{HCO}^+} = 1 \times 10^{16} \text{ cm}^{-2}$, $[\text{HCN}]/[\text{HCO}^+] = 3$, and observed high-J to low-J flux ratios. The density and temperature are well constrained.

In Figure 3, the observed HCN-to-HCO⁺ flux ratio for the two sources located at the bottom left part, including NGC 1614, can also be explained by a non-enhanced HCN-to-HCO⁺ abundance ratio ($[\text{HCN}]/[\text{HCO}^+] = 1$). Furthermore, it is possible that the LIRG NGC 1614 has lower column density than those of ULIRGs. Thus, the same least-squares fit is conducted by adopting (1) $[\text{HCN}]/[\text{HCO}^+] = 1$ (Figure 4b), and (2) $N_{\text{HCO}^+} = 1 \times 10^{15} \text{ cm}^{-2}$, in addition to $[\text{HCN}]/[\text{HCO}^+] = 1$ (Figure 4c). Only a limited change in the derived H₂ molecular gas density (n_{H_2}) and temperature (T_{kin}) is observed.

In contrast to the HCN-to-HCO⁺ flux ratios for the same J transition where both HCN and HCO⁺ data were obtained simultaneously, the high-J to low-J flux ratios of HCN and HCO⁺ are affected by the possible absolute flux calibration uncertainty of individual ALMA observations. This is because data for J=4-3, J=3-2, and J=2-1 were obtained at different times. Therefore, this possible systematic uncertainty must be considered. The absolute flux calibration uncertainty is as high as

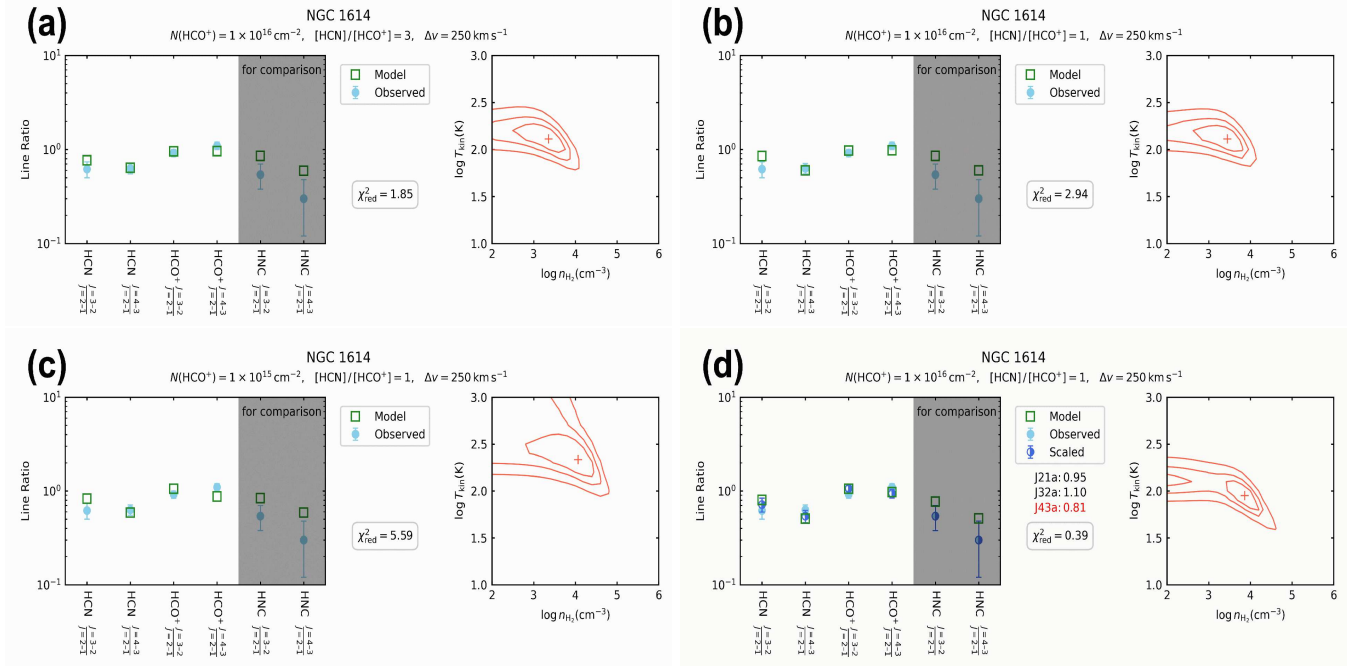


Figure 4. Example of fitting results for the high-J to low-J flux ratios of HCN and HCO⁺ for the starburst-dominated LIRG NGC 1614. HCO⁺ column density and HCN-to-HCO⁺ abundance ratio are (a): ($N_{\text{HCO}^+}/\text{cm}^2$, $[\text{HCN}]/[\text{HCO}^+]$) = (1×10^{16} , 3), (b): (1×10^{16} , 1), (c): (1×10^{15} , 1), and (d): (1×10^{16} , 1) with scaling factor adjustment allowed. The line width is fixed at $\Delta v = 250 \text{ km s}^{-1}$ for all cases. (*Left panel of each plot*): Comparison of the observed and modeled line flux ratios. The green open squares represent the best-fit RADEX model. Its gas density and temperature values are indicated by the plus sign in the right panel, whereas other fixed parameters (HCO⁺ column density, HCN-to-HCO⁺ abundance ratio, and line width) are listed at the top of the figure below the object name. The light blue filled circles represent the flux ratios measured from our observations. In (d), the dark blue half-filled circles represent the flux ratios by allowing scale adjustment within the absolute flux calibration uncertainty of individual ALMA observations. Below the legend, the scaling factors to be multiplied for the line fluxes are listed. If a factor is colored red, it implies that the observation was made in Cycle 0 (double systematic error). For example, in (d), the J=3–2 to J=2–1 flux ratios are multiplied by a factor of $1.10/0.95 = 1.16$. In (a)–(d), the reduced χ^2 value for the best-fit model is listed at the bottom middle part. The HNC line flux ratios in the shaded part of the left panel are shown only for reference and are not used in the fitting; the HNC abundance is assumed to be equal to that of HCO⁺. (*Right panel*): Confidence ranges for gas density and temperature. The plus sign indicates the position of the best-fit model. The contours represent 68, 90, and 99% confidence levels for the two parameters of interest ($\Delta\chi^2 = 2.28, 4.61, 9.21$).

5% for J21a⁴ (band 5) and 10% for J32a and J43a (bands 6 and 7), respectively, according to the ALMA Proposer’s Guide. However, for Cycle 0 observations, we conservatively choose to adopt twice the above values, because of possibly large systematic uncertainty in ALMA very early phase. We allow scaling of the absolute fluxes within the above range. If individual emission line fluxes are scaled, then their flux ratios will change accordingly.

⁴ See Table 2 caption for the definition of J21a, J32a, and J43a.

We adopt two steps. First, in addition to gas density (n_{H_2}) and temperature (T_{kin}), the scaling factors for J21a, J32a, and J43a are treated as free parameters that move within the systematic uncertainty. Least-squares fitting with box constraints is performed with L-BFGS-B algorithm (Byrd et al. 1995). Subsequently, the scaling factors are fixed at the determined values. Then, gas density and temperature are derived using the Levenberg-Marquardt algorithm in the same manner as before. Figure 4d shows the results obtained by allowing the flux scale adjustment. The best fit values based on the four models in Figure 4 are summarized in Table 6. The derived gas density and temperature largely agree in the range $n_{\text{H}_2} = 10^{3.4-4.1} \text{ cm}^{-3}$ and $T_{\text{kin}} = 10^{2.0-2.3} \text{ K}$ for all the methods in Figure 4.

Figure 4 shows that the derived gas density and temperature are not strongly dependent on the choice of the HCN-to-HCO⁺ abundance ratio ($[\text{HCN}]/[\text{HCO}^+]$) and HCO⁺ column density (N_{HCO^+}). Thus, we perform the same fit for the remaining ULIRGs by adopting the fiducial values of $[\text{HCN}]/[\text{HCO}^+] = 3$ and $N_{\text{HCO}^+} = 1 \times 10^{16} \text{ cm}^{-2}$. We adopt the line widths (Δv) listed in Table 3 (column 11) which are not the same among individual ULIRGs. As in the case of NGC 1614, we (1) use the observed high-J to low-J flux ratios as they are, and (2) allow scale adjustment for individual J=4–3, J=3–2, and J=2–1 data to consider the possible absolute flux calibration uncertainty of individual ALMA observations. The derived gas density and temperature largely agree between the first and second fitting results, although the second one usually provides a smaller reduced χ^2 value than the former. We basically adopt the first fitting result, but do the second one only if the first one cannot determine the most likely value or gives a very large reduced χ^2 value. Figure 5 shows our adopted result for each ULIRG’s nucleus. Table 6 summarizes the best fit values for the ULIRGs.

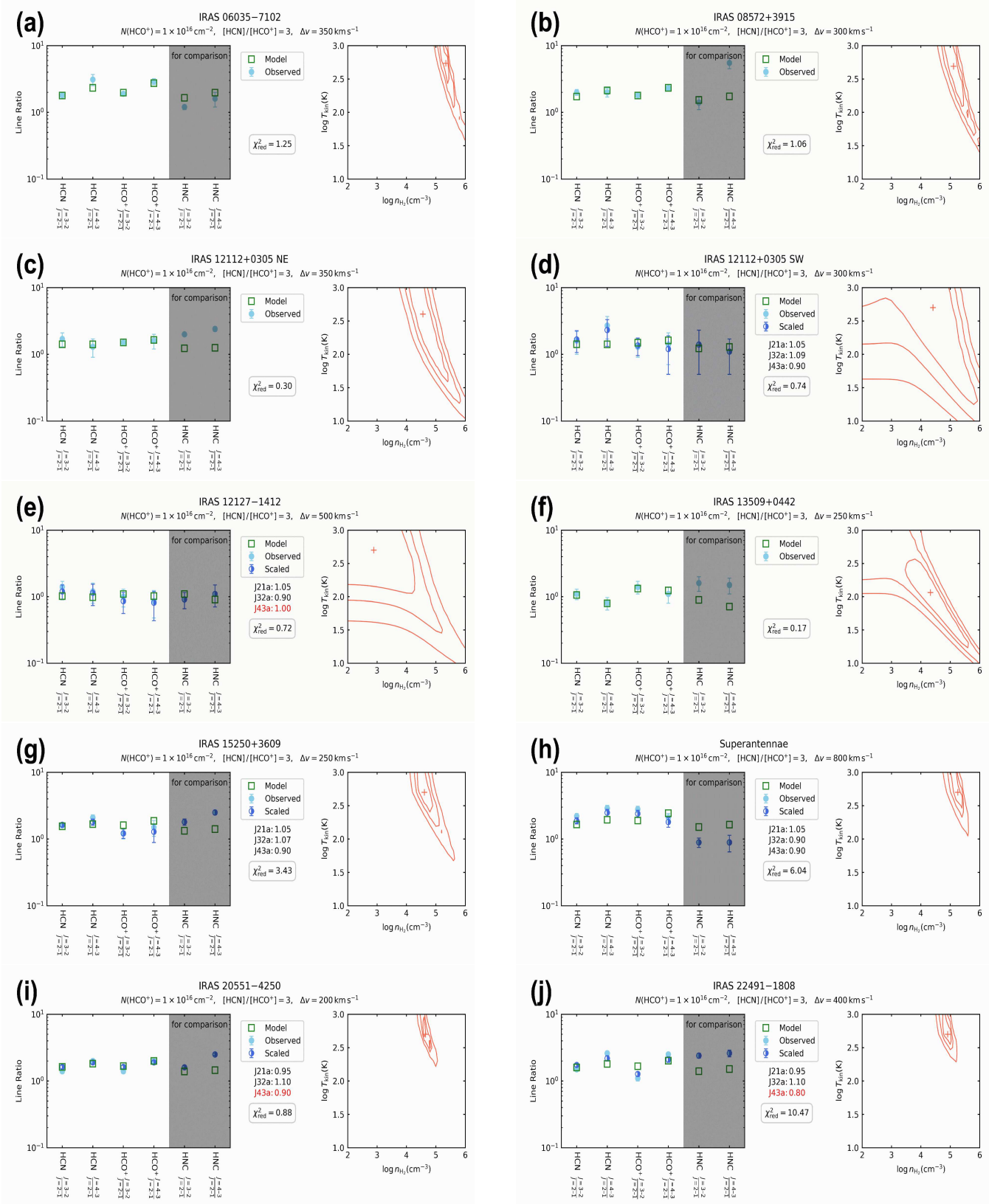


Figure 5. Same as Figure 4, but for ULIRGs’ nuclei. HCO^+ column density of $N_{\text{HCO}^+} = 1 \times 10^{16} \text{ cm}^{-2}$ and HCN-to- HCO^+ abundance ratio of $[\text{HCN}]/[\text{HCO}^+] = 3$ are assumed for all the sources. Line widths (Δv) are different among different ULIRGs and are presented in Table 3 (Column 11). Symbols are the same as those in Figure 4. We adopt the second fitting result (that is, flux-scaling adjustment allowed) for IRAS 12112+0305 SW, IRAS 12127–1412, IRAS 15250+3609, the Superantennae, IRAS 20551–4250, and IRAS 22491–1808.

Table 6. Summary of the Best Fit Values

Object	$\log N_{\text{HCO}^+}$ [cm ⁻²]	[HCN]/[HCO ⁺]	Scaling	$\log n_{\text{H}_2}$ [cm ⁻³]	$\log T_{\text{kin}}$ [K]	Reduced χ^2	Remark
(1)	(2)	(3)	(4)	(5)	(6)	(7)	(8)
NGC 1614	16	3	off	$3.4^{+0.3}_{-0.5}$	2.1 ± 0.1	1.9	Figure 4a
	16	1	off	$3.4^{+0.3}_{-0.4}$	2.1 ± 0.1	2.9	Figure 4b
	15	1	off	$4.1^{+0.3}_{-0.6}$	$2.3^{+0.2}_{-0.1}$	5.6	Figure 4c
IRAS 06035–7102	16 ($16.0^{+0.4}_{-0.5}$)	1 (3.5 ± 0.5)	on (on)	$3.9^{+0.2}_{-0.3}$ (3.3 ± 0.8)	2.0 ± 0.1 (2.0 ± 0.2)	0.39 (1.0)	Figure 4d,7a
	16 ($16.6^{+0.3}_{-0.4}$)	3 ($4.7^{+1.1}_{-1.4}$)	off (on)	5.3 ± 0.2 ($5.5^{+0.3}_{-0.4}$)	$2.7^{+0.0}_{-0.3}$ ($2.0^{+0.6}_{-0.3}$)	1.3 (4.2)	Figure 5a,7b
IRAS 08572+3915	16 ($16.4^{+0.4}_{-0.5}$)	3 ($4.9^{+1.3}_{-1.5}$)	off (on)	5.1 ± 0.3 ($5.2^{+0.4}_{-0.5}$)	$2.7^{+0.0}_{-0.5}$ ($2.0^{+0.6}_{-0.4}$)	1.1 (1.7)	Figure 5b,7c
IRAS 12112+0305 NE	16 ($15.7^{+0.8}_{-1.0}$)	3 ($8.7^{+1.0}_{-1.4}$)	off (on)	$4.6^{+0.5}_{-0.4}$ ($4.6^{+0.4}_{-0.7}$)	$2.6^{+0.0}_{-0.7}$ ($2.7^{+0.2}_{-0.3}$)	0.30 (2.1)	Figure 5c,7d
IRAS 12112+0305 SW	16	3	on	$4.4^{+0.6}_{-0.7}$	$2.7^{+0.0}_{-0.7}$	0.74	Figure 5d
IRAS 12127–1412	16	3	on	$2.9^{+1.1}_{-0.0}$	$2.7^{+0.0}_{-0.4}$	0.72	Figure 5e
IRAS 13509+0442	16 (15.7 ± 0.8)	3 ($6.3^{+1.9}_{-2.2}$)	off (on)	$4.3^{+1.0}_{-0.5}$ ($4.3^{+0.9}_{-1.2}$)	$2.1^{+0.3}_{-0.7}$ (2.1 ± 0.6)	0.17 (1.3)	Figure 5f,7e
IRAS 15250+3609	16	3	on	4.6 ± 0.2	$2.7^{+0.3}_{-0.2}$	3.4	Figure 5g
Superantennae	16	3	on	$5.3^{+0.1}_{-0.2}$	$2.7^{+0.3}_{-0.1}$	6.0	Figure 5h
IRAS 20551–4250	16 ($15.4^{+0.6}_{-0.2}$)	3 (2.9 ± 0.2)	on (on)	4.6 ± 0.1 ($4.5^{+0.3}_{-0.2}$)	$2.7^{+0.2}_{-0.1}$ ($2.8^{+0.1}_{-0.2}$)	0.88 (8.3)	Figure 5i,7f
IRAS 22491–1808	16	3	on	4.9 ± 0.1	$2.7^{+0.3}_{-0.1}$	10.5	Figure 5j

NOTE— Col.(1): Object name. Col.(2): Decimal logarithm of HCO⁺ column density in units of cm⁻². Col.(3): HCN-to-HCO⁺ abundance ratio. Col.(4): Scaling on or off. Col.(5): Decimal logarithm of H₂ gas density in units of cm⁻³. Col.(6): Decimal logarithm of gas kinetic temperature in units of K. In Cols.(2)–(6), the best fit values based on the Bayesian method (§5.5) are displayed in parentheses for selected (U)LIRGs. For very high HCO⁺ column density and HCN-to-HCO⁺ abundance ratio, HCN emission line becomes very optically thick and its flux does not change. Thus, some of the derived HCO⁺ column density and/or HCN-to-HCO⁺ abundance ratio could be lower limits. Col.(7): Reduced χ^2 value. Col.(8): Remark. Corresponding figure information is added.

5.4. Overall Trend of Molecular Gas Properties at (U)LIRGs' Nuclei

In Figure 5, the uncertainty in the derived gas density and temperature is large for IRAS 12112+0305 SW and IRAS 12127–1412 simply because molecular line emission is fainter than other (U)LIRGs' nuclei (Figure 1). Excluding these two ULIRGs' nuclei, we see the following two trends in Figures 4 and 5; (1) The only one LIRG NGC 1614 contains nuclear molecular gas with modestly high density ($10^{3.4-4.1} \text{ cm}^{-3}$) and high temperature (100–200 K or $10^{2.0-2.3}$ K). (2) Nuclear molecular gas probed with HCN and HCO^+ at J=2–1 to J=4–3 in all ULIRGs but IRAS 13509+0442 is significantly denser ($10^{4.5-5.5} \text{ cm}^{-3}$) and warmer ($\gtrsim 300$ K or $\gtrsim 10^{2.5}$ K) than that in the LIRG NGC 1614. These two results constitute our first main arguments. The gas density and temperature at these ULIRGs' nuclei are also systematically higher than those of other LIRGs in the literature, derived from larger beam-sized CO multiple J-transition (J=1–0 to J=6–5) line data and RADEX modeling (mostly $10^{2.0-4.0} \text{ cm}^{-3}$ and 10–90 K) (e.g., Papadopoulos et al. 2012b). IRAS 13509+0442 has relatively low density ($\sim 10^{4.3} \text{ cm}^{-3}$) and temperature (~ 130 K or $\sim 10^{2.1}$ K) nuclear molecular gas compared to other ULIRGs. Although there are certain difference among the observed sources, the derived gas density and temperature of all (U)LIRGs' nuclei are substantially higher than those of quiescently star-forming, less infrared luminous galaxies at $\lesssim \text{kpc}$ scale, suggested from the observed small high-J to low-J emission line flux ratios of HCN and HCO^+ (Garcia-Rodriguez et al. 2023) or derived from CO multiple J-transition (J=1–0 to J=3–2) line data and RADEX modeling with fixed $N_{\text{CO}}/\Delta v$ ratio ($\lesssim 10^{4.0} \text{ cm}^{-3}$ and $\lesssim 50$ K) (e.g., Leroy et al. 2022).

NGC 1614 and IRAS 13509–0442, together with IRAS 12112+0305 SW, are classified as starburst-dominated with no luminous AGN signature at any wavelength, whereas the remaining ULIRGs are regarded as containing luminous AGNs based on previous observations (§2). In other words, there is a trend that nuclear molecular gas is denser and warmer in ULIRGs with luminous AGN signatures than in (U)LIRGs without. This is our second main argument. Figure 6 shows the contours of the derived gas density and temperature for (U)LIRGs with small uncertainty (excluding IRAS 12112+0305 SW and IRAS 12127–1412). It has previously been suggested that AGN activity is enhanced in galaxy nuclei with a larger amount of and/or higher fraction of dense molecular gas (Juneau et al. 2009; Izumi et al. 2016b). This appears reasonable because the mass accretion rate onto a SMBH is enhanced by a larger amount of dense molecular gas near the SMBH. Owing to the high SMBH mass accretion, luminous AGN activity can emerge and make the surrounding dense molecular gas warm. The second argument can be explained naturally by the combination of these two effects.

For the three ULIRGs, IRAS 08572+3915, IRAS 12112+0305, and IRAS 22491–1808, molecular gas temperature was estimated to be 60–150 K, based on large beam-sized CO multiple J-transition line observations and RADEX modeling (Papadopoulos et al. 2012a). Our ALMA HCN and HCO^+ line study provides significantly higher temperature for nuclear molecular gas in all the three ULIRGs (see Figure 5 and Table 6). This suggests that our ALMA 1–2 kpc resolution dense molecular line observations selectively probe warm nuclear molecular gas components around luminous energy sources with minimum contamination from spatially extended ($\gtrsim \text{a few kpc}$) cool components. This advantage was also demonstrated in ALMA high-spatial-resolution HCN and HCO^+ observations of the nearby well-studied, optically identified AGN NGC 1068, to probe molecular gas only in the vicinity of a luminous energy source (e.g., Viti et al. 2014). Baba et al. (2018) revealed the presence of high temperature ($\gtrsim 200$ K) molecular gas at the innermost part of obscuring material around

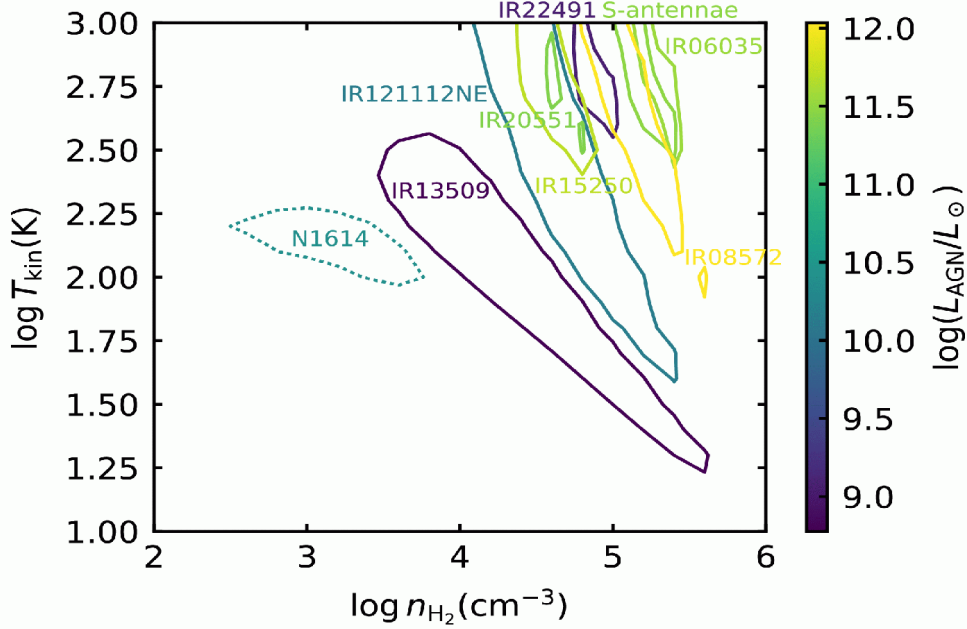


Figure 6. Summary of contours of the RADEX-derived molecular gas density in cm^{-3} (abscissa) and temperature in K (ordinate) for the observed (U)LIRGs, excluding the two faint molecular emission line ULIRGs (IRAS 12112+0305 SW and IRAS 12127–1412). Color corresponds to infrared-derived AGN luminosity in units of solar luminosity (L_{\odot}), as listed in Table 1 (columns 9 and 11). NGC 1614 is shown as a dotted line because the upper limit of AGN luminosity is looser than that of other ULIRGs. For all the ULIRGs, the AGN luminosity is derived by Nardini et al. (2010) in a consistent manner, whereas that of NGC 1614 is estimated in a different method by a different group (Pereira-Santaella et al. 2015).

luminous AGNs in nearby ULIRGs, based on the observed properties of $\sim 4.6 \mu\text{m}$ CO ro-vibrational absorption lines detected in the infrared 4–5 μm spectra. It is likely that HCN and HCO^+ rotational emission at $J=2-1$ to $J=4-3$ detected in our ALMA high-angular-resolution observations largely originates from such innermost high temperature molecular gas at nearby ULIRGs’ nuclei.

5.5. Bayesian Analysis of Molecular Emission Line Flux Ratios

For selected (U)LIRGs’ nuclei exhibiting bright molecular emission lines with high detection significance, molecular gas parameters are estimated by simultaneously fitting HCN-to- HCO^+ and high-J to low-J emission line flux ratios using RADEX calculations, by making all parameters free, based on a Bayesian approach. The aim is to verify whether the Bayesian approach provides consistent results regarding gas density and temperature with those derived from the previous Levenberg-Marquardt method, where the HCO^+ column density and HCN-to- HCO^+ abundance ratios were fixed to fiducial values (§5.3). There are five independent emission line flux ratios (HCN-to- HCO^+ flux ratios at $J=2-1$, $J=3-2$, and $J=4-3$, and HCO^+ $J=3-2$ to $J=2-1$ and $J=4-3$ to $J=2-1$ flux ratios), which are lower than the total number of parameters, including the absolute flux calibration scaling factors. However, Bayesian estimation facilitates the sampling of the posterior probability distribution of parameters, considering indeterminacy of the solution.

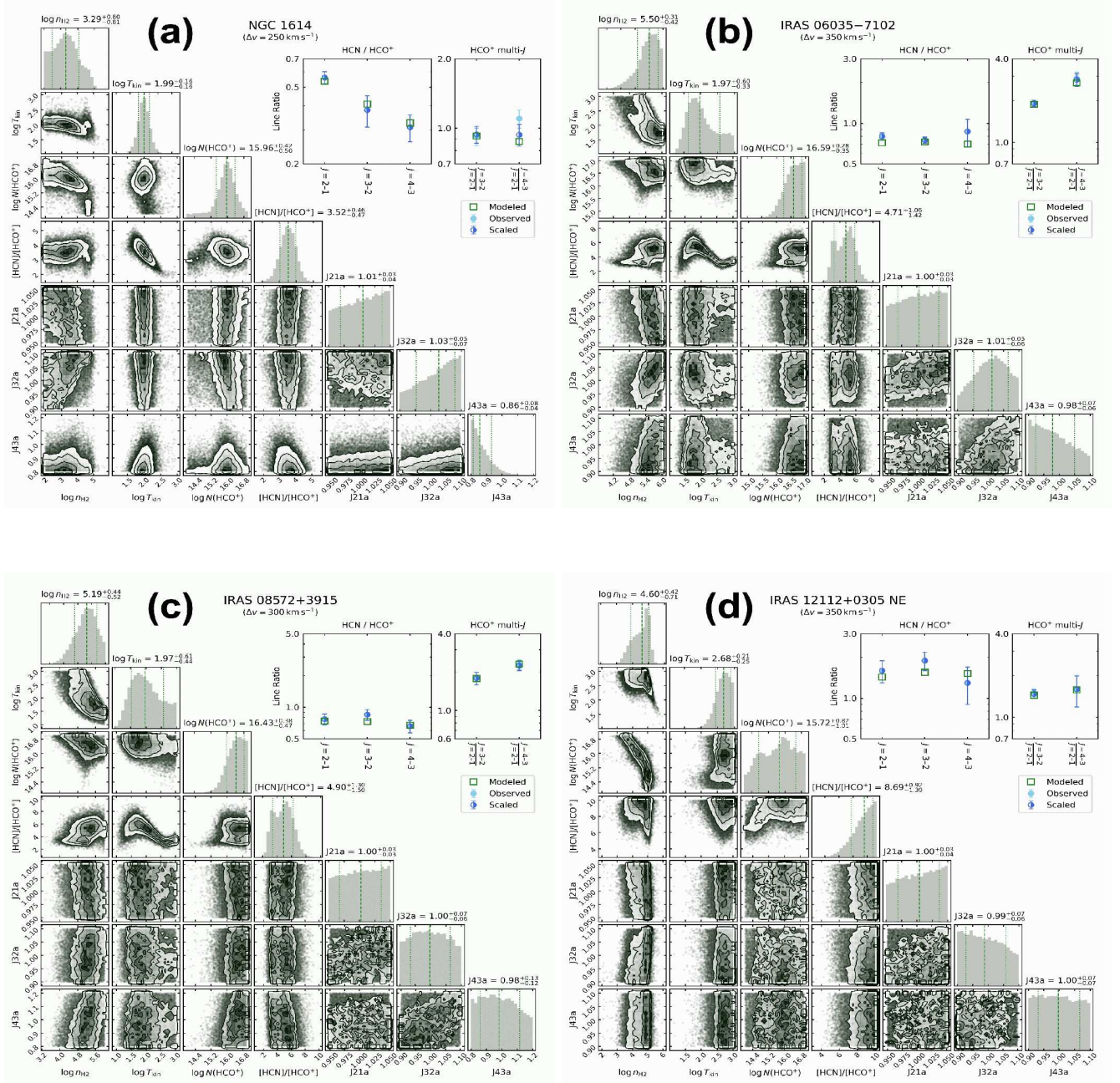
Using the five emission line flux ratios, we explore the parameter space using a Markov Chain Monte Carlo (MCMC) sampler; `emcee` package (Foreman-Mackey et al. 2013) is used in `lmfit`. Flat priors with upper and lower bounds presented in Table 7 are adopted. The first guess is made by running the L-BFGS-B solver in §5.3, with the HCO^+ column density and HCN-to- HCO^+ abundance ratio unfixed, and then 100 walkers are initialized to be distributed around that guess. The chain is run for 100τ steps, where τ is the maximum number of integrated autocorrelation time for each parameter⁵. The first 5τ steps are discarded as a “burn-in” phase. Subsequently, the chain is thinned out in 0.5τ steps to create independent samples. Hence, the effective number of sampling of the posterior probability distribution is $100 \times (100 - 5)/0.5 = 19,000$.

For our MCMC analysis, IRAS 12112–1412 SW and IRAS 12127–1412 are excluded, because of their faint molecular emission lines. Examples of the MCMC analysis results for six selected (U)LIRGs’ nuclei are shown in Figure 7 and the best fit values are summarized in Table 6. Results for IRAS 15250+3609, the Superantennae, and IRAS 22491–1808 are not shown because we are unable to provide model-calculated results which reproduce the observed results very well with small systematic discrepancy. This independent MCMC analysis supports the previous arguments that (1) molecular gas at the (U)LIRGs’ nuclei is dense ($\gtrsim 10^{3-4} \text{ cm}^{-3}$) and warm ($\gtrsim 100 \text{ K}$) compared to quiescently star-forming normal galaxies with less infrared luminosity and (2) the density of nuclear molecular gas is higher in ULIRGs ($\gtrsim 10^{4.3} \text{ cm}^{-3}$) than in the LIRG NGC 1614 ($\sim 10^{3.3} \text{ cm}^{-3}$).

Table 7. Bounds of the Flat Priors

Parameter	Lower	Upper
$\log(n_{\text{H}_2}/\text{cm}^{-3})$	2	6
$\log(T_{\text{kin}}/\text{K})$	1	3
$\log(N_{\text{HCO}^+}/\text{cm}^{-2})$	14	17
$[\text{HCN}]/[\text{HCO}^+]$	0.1	10
J21a scaling	0.95	1.05
J32a scaling	0.9	1.1
J43a scaling	0.9	1.1

⁵ Ideally, τ should be derived from a chain of infinite lengths. In our framework, τ generally increases with the number of steps in the chain (N) and converges asymptotically to a reliable value. Therefore, we lengthen the chain while monitoring τ and terminate the calculation when N/τ exceeds 100. This is a more conservative option than the minimum chain length recommended in the `emcee` documentation ($N/\tau = 50$).



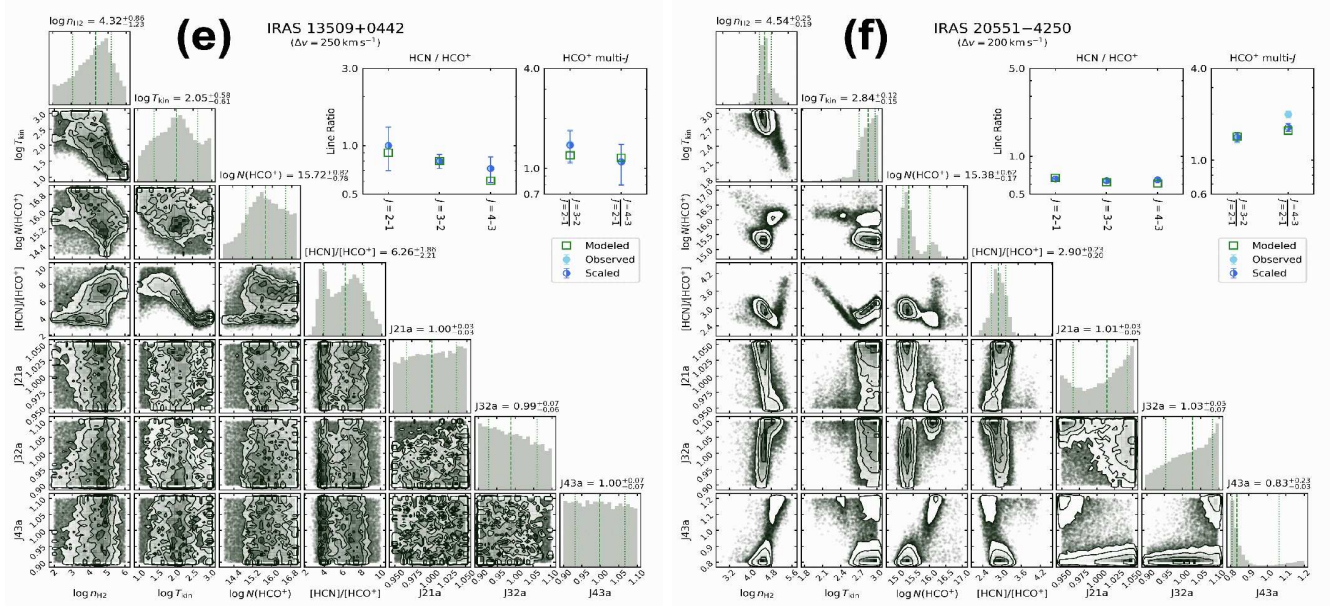


Figure 7. Example results of the MCMC analysis of the HCN-to-HCO⁺ line flux ratios and HCO⁺ high-J to low-J line flux ratios. Shown in the left is a corner plot which displays the posterior probability distribution of each parameter and the covariance of each parameter pair as 1D and 2D histograms, respectively. The median and 68% credible bounds for each parameter posterior are indicated by the vertical dashed and dotted lines, respectively, and are also given in the panel title. A comparison of the line flux ratios is shown in the upper right panel. The green open squares show the model flux ratios calculated at the medians of $\log n_{\text{H}_2}$, $\log T_{\text{kin}}$, $\log N_{\text{HCO}^+}$, and $[\text{HCN}]/[\text{HCO}^+]$. The light blue filled circles indicate the flux ratios as observed and the dark blue half-filled circles indicate line flux ratios scaled from the observed values using the medians of the scaling factors for J21a, J32a, and J43a. The residuals used for the likelihood are the differences between the model and scaled line flux ratios, normalized by the statistical uncertainty in the latter ratio.

6. SUMMARY

We presented our ALMA $\lesssim 1\text{--}2$ kpc-resolution observational results of dense molecular gas tracers (HCN, HCO^+ , and HNC) at multiple rotational transition lines ($J=2\text{--}1$, $3\text{--}2$, and $4\text{--}3$) for one LIRG NGC 1614 ($L_{\text{IR}} \sim 10^{11.7} L_{\odot}$) and nine ULIRGs ($L_{\text{IR}} = 10^{12.0\text{--}12.3} L_{\odot}$). The beam sizes of all the molecular J-transition lines obtained with different beams (different array configurations) were matched to the same value (1–2 kpc) for each (U)LIRG. Thereafter, the high-J to low-J emission line flux ratios for each molecule and emission line flux ratios among the different molecules at each J-transition were derived. Based primarily on the HCN and HCO^+ data which can probe the properties of dense and warm molecular gas near luminous energy sources, the observational and RADEX non-LTE modeling results were compared to constrain H_2 gas volume number density and kinetic temperature in these (U)LIRGs’ nuclear 1–2 kpc regions. We obtained the following main results.

1. HCN and HCO^+ line emission was significantly detected at up to $J=4\text{--}3$, suggesting that dense and warm molecular gas is abundant in the observed (U)LIRGs’ nuclei.
2. The overall distribution of the observed HCN-to- HCO^+ flux ratios at $J=2\text{--}1$, $J=3\text{--}2$, and $J=4\text{--}3$ for the (U)LIRGs’ nuclei were better reproduced by enhanced HCN abundance, relative to HCO^+ , although the ratios in a few sources could be explained by comparable HCN and HCO^+ abundance.
3. We applied the Levenberg-Marquardt method for all the (U)LIRGs’ nuclei by adopting fiducial values for molecular column density and HCN-to- HCO^+ abundance ratio. Consequently, it was quantitatively derived that molecular gas in the observed (U)LIRGs’ nuclei was generally dense ($\gtrsim 10^{3\text{--}4} \text{ cm}^{-3}$) and warm ($\gtrsim 100$ K). This conclusion was confirmed to be insensitive to the choice of the fiducial values.
4. The only one observed LIRG NGC 1614 showed molecular gas density and temperature distinctly lower than those of the remaining nine ULIRGs. However, the derived gas density and temperature in all the observed (U)LIRGs’ nuclei, including NGC 1614, were substantially higher than those in quiescently star-forming normal galaxies with even less infrared luminosity.
5. For selected (U)LIRGs’ nuclei with bright molecular line emission, we also applied a Bayesian approach to constrain molecular gas properties, with all parameters set as free, by using the Markov Chain Monte Carlo (MCMC) method. The above arguments 3 and 4 were supported.
6. The derived density and temperature of nuclear molecular gas in starburst-dominated sources tended to be lower than those of the majority of ULIRGs that exhibited signatures of luminous AGNs from infrared, hard X-ray (>10 keV), and (sub)millimeter spectroscopic observations. This conformed to previous suggestions that luminous AGN activity was associated with a larger amount of and/or higher fraction of nuclear dense molecular gas.

This study demonstrated that high-spatial-resolution ($\lesssim 1\text{--}2$ kpc) ALMA observations of multiple dense molecular gas tracers at multiple J-transition lines are an effective tool for quantitatively constraining molecular gas properties of (U)LIRGs’ nuclei, by minimizing possible contamination from spatially extended (\gtrsim a few kpc), more diffuse and cooler molecular gas emission in the host galaxies.

We thank the anonymous referee for valuable comment which helped improve the clarity of this manuscript. This paper made use of the following ALMA data: ADS/JAO.ALMA#2011.0.00020.S, #2013.1.00032.S, #2013.1.00033.S, #2015.1.00027.S, #2017.1.00022.S and #2017.1.00023.S. ALMA is a partnership of ESO (representing its member states), NSF (USA) and NINS (Japan), together with NRC (Canada), NSC and ASIAA (Taiwan), and KASI (Republic of Korea), in cooperation with the Republic of Chile. The Joint ALMA Observatory is operated by ESO, AUI/NRAO, and NAOJ. M.I., K.N., and T.I. are supported by JP21K03632, JP19K03937, and JP20K14531, respectively. S.B. is supported by JP19J00892 and JP21H04496. Data analysis was in part carried out on the open use data analysis computer system at the Astronomy Data Center, ADC, of the National Astronomical Observatory of Japan. This research has made use of NASA’s Astrophysics Data System and the NASA/IPAC Extragalactic Database (NED) which is operated by the Jet Propulsion Laboratory, California Institute of Technology, under contract with the National Aeronautics and Space Administration.

Facilities: ALMA

Software: RADEX (van der Tak et al. 2007), CASA (THE CASA Team 2022), pyradex (<https://github.com/keflavich/pyradex>), IPython (Perez & Granger 2007), Jupyter Notebook (Kluyver et al. 2016), NumPy (Harris et al. 2020), SciPy (Virtanen et al. 2020), Pandas (Reback et al. 2022), Matplotlib (Hunter 2007), Astropy (Astropy Collaboration et al. 2022), lmfit (Newville et al. 2021), emcee (Foreman-Mackey et al. 2013), corner (Foreman-Mackey 2016)

APPENDIX

A. PREVIOUSLY UNPUBLISHED OBSERVATION DETAILS AND OBTAINED SPECTRA OF TWO ULTRALUMINOUS INFRARED GALAXIES

Table 8 summarizes the log of previously unpublished ALMA Cycle 5 observations for the two ULIRGs, IRAS 06035–7102 and IRAS 08572+3915. The obtained spectra are shown in Figure 8.

Table 8. Observation Log of Two ULIRGs

Object	Line	Date	Antenna	Baseline	Integration	Calibrator		
		[UT]	Number	[m]	[min]	Bandpass	Flux	Phase
(1)	(2)	(3)	(4)	(5)	(6)	(7)	(8)	(9)
IRAS 06035–7102	HCN and HCO ⁺ J=4–3	2017 December 26	46	15–2517	15	J0522–3627	J0522–3627	J0529–7245
	HNC J=4–3	2017 December 12	45	15–3321	12	J0522–3627	J0522–3627	J0529–7245
IRAS 08572+3915	HNC J=4–3	2017 December 26	46	15–2517	19	J0854+2006	J0854+2006	J0916+3854
		2017 December 31	47	15–2517	19	J0854+2006	J0854+2006	J0916+3854
		2018 January 22	45	15–1398	19	J0854+2006	J0854+2006	J0916+3854

NOTE— Col.(1): Object name. Col.(2): Observed molecular line. Col.(3): Observation date in UT. Col.(4): Number of antennas used for observations. Col.(5): Baseline length in meters. The minimum and maximum baseline lengths are shown. Col.(6): Net on source integration time in minutes. Cols.(7), (8), and (9): Bandpass, flux, and phase calibrator for the target source, respectively.

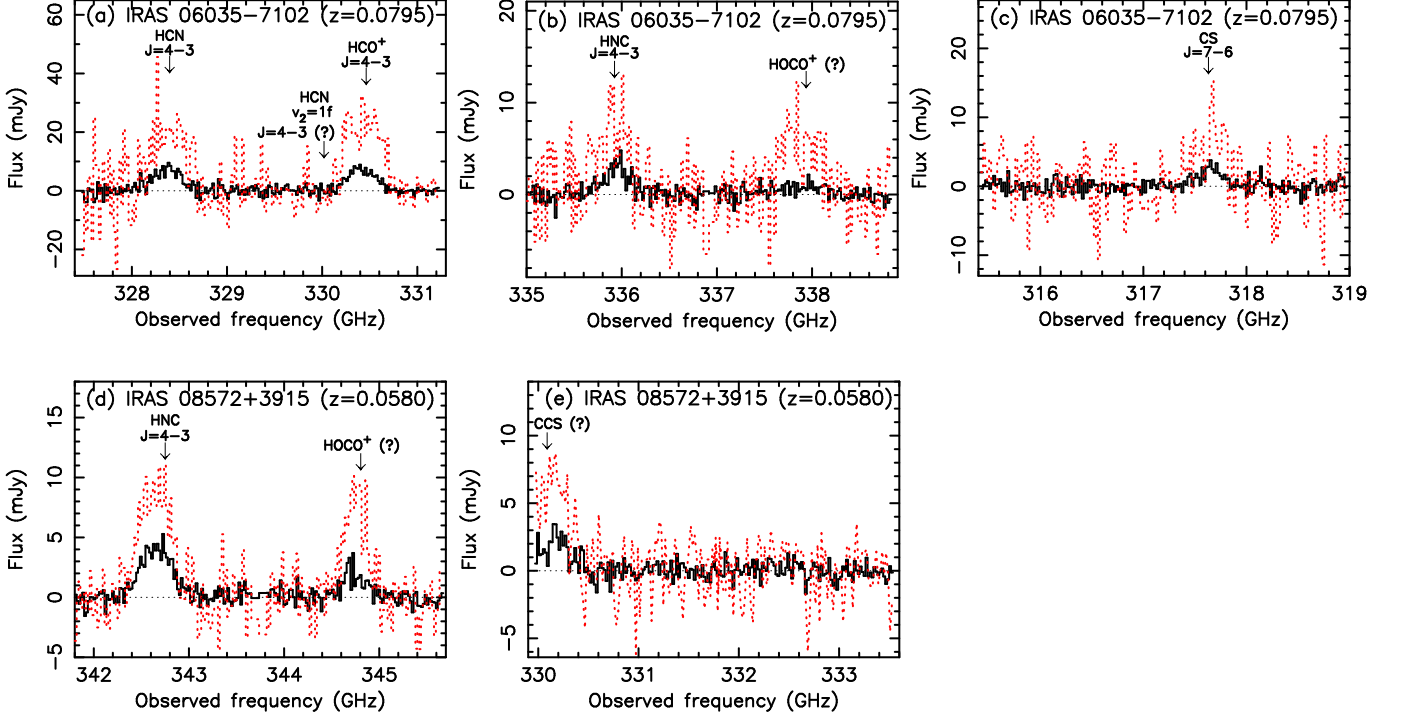


Figure 8. ALMA band 7 (275–373 GHz) spectra obtained in Cycle 5. The abscissa is the observed frequency in GHz, and the ordinate is the flux density in mJy. IRAS 06035–7102 spectra of (a) J43a USB (including HCN and HCO⁺ J=4–3), (b) J43b LSB (including HNC J=4–3), and (c) J43a LSB (including CS J=7–6). IRAS 08572+3915 spectra of (d) J43b USB (including HNC J=4–3) and (e) J43b LSB. Black solid line: original beam-sized spectrum (Table 2). Red dotted line: 1.6 kpc and 1 kpc beam spectra for (a–c) IRAS 06035–7102 and (d–e) IRAS 08572+3915, respectively. The horizontal black thin dotted straight line indicates the zero flux level. In (b) and (d), a serendipitously detected modestly bright emission line is tentatively identified as HOCO⁺ 17(1,16)–16(1,15) at $\nu_{\text{rest}} = 364.804$ GHz. In (e), a serendipitously detected modestly bright emission line is tentatively identified as CCS N=27–26, J=26–25 at $\nu_{\text{rest}} = 349.234$ GHz. IRAS 06035–7102 J43b USB spectrum is not shown because no emission line signature is seen.

B. GAUSSIAN FITTING RESULTS OF MOLECULAR EMISSION LINES

Our final Gaussian fitting results for molecular emission lines are summarized in Table 9. In Figures 9 and 10, we overplot adopted Gaussian profiles on the observed data to see the goodness of the fits.

Table 9. Gaussian Fit of Dense Molecular Emission Lines

Object	Molecule	Line	Gaussian fit			
			Velocity [km s ⁻¹]	Peak [mJy]	FWHM [km s ⁻¹]	Flux [Jy km s ⁻¹]
(1)	(2)	(3)	(4)	(5)	(6)	(7)
NGC 1614 (1 kpc)	HCN	J=2-1	4765±4	27±1	243±10	6.8±0.4
		J=3-2	4776±14	16±2	245±34	4.2±0.8
		J=4-3	4769±10	16±1	252±24	4.3±0.5
	HCO ⁺	J=2-1	4769±4	47±1	252±8	12±1
		J=3-2	4757±8	42±3	256±13	11±1
		J=4-3	4773±7	55±3	240±16	14±1
	HNC	J=2-1	4766±8	16±1	222±17	3.7±0.4
		J=3-2	4782±24	7.0±1.3	273±60	2.0±0.6 ^A
		J=4-3	4740±32	4.3±1.8	245±94	1.1±0.6 ^A
IRAS 06035-7102 (1.6 kpc)	HCN	J=2-1	23857±5	7.8±0.2	371±11	2.9±0.1
		J=3-2	23852±5	14±1	366±12	5.1±0.2
		J=4-3	23847±26	23±3	383±62	8.8±1.8
	HCO ⁺	J=2-1	23867±5	8.9±0.2	404±13	3.6±0.1
		J=3-2	23867±4	18±1	383±9	6.8±0.2
		J=4-3	23858±13	27±2	383±34	10±1
	HNC	J=2-1	23832±11	4.6±0.3	356±25	1.6±0.1
		J=3-2	23833±9	5.9±0.3	330±20	1.9±0.2
		J=4-3	23844±24	8.1±1.2	328±64	2.6±0.6
IRAS 08572+3915 (1 kpc)	HCN	J=2-1	17485±11	3.6±0.2	383±27	1.4±0.1
		J=3-2	17489±9	7.7±0.4	363±22	2.8±0.2
		J=4-3	17476±13	7.6±0.6	367±31	2.8±0.3
	HCO ⁺	J=2-1	17480±7	5.5±0.2	332±17	1.8±0.1 ^A
		J=3-2	17485±8	11±1	292±17	3.3±0.3
		J=4-3	17489±13	15±1	289±15	4.2±0.3
	HNC	J=2-1	17481±16	1.9±0.2	315±33	0.61±0.09
		J=3-2	17493±14	3.0±0.3	278±33	0.84±0.13
		J=4-3	17489±11	9.6±0.6	346±24	3.3±0.3
IRAS 12112+0305 NE (1.5 kpc)	HCN	J=2-1	21811±4, 21790±5	17±2, -7.5±2.2 ^B	395±16, 180±21	5.5±1.0
		J=3-2	21641±18, 21931±23	14±2, 18±1	253±30, 327±52	9.4±1.2
		J=4-3	21687±48, 21970±10	13±1, 18±3	316±101, 164±43	7.2±1.7
	HCO ⁺	J=2-1	21661±7, 21955±7	7.5±0.4, 8.4±0.4	201±18, 229±21	3.4±0.3
		J=3-2	21671±9, 21965±7	12±1, 14±1	188±4, 202±18	5.0±0.4
		J=4-3	21656±21, 21989±12	11±2, 15±2	226±61, 201±54	5.5±1.2
	HNC	J=2-1	21805±6	12±1	352±14	4.3±0.2

Table 9 continued on next page

Table 9 (*continued*)

Object	Molecule	Line	Gaussian fit			
			Velocity	Peak	FWHM	Flux
			[km s ^{−1}]	[mJy]	[km s ^{−1}]	[Jy km s ^{−1}]
(1)	(2)	(3)	(4)	(5)	(6)	(7)
IRAS 12112+0305 SW (1.5 kpc)	HCN	J=3–2	21796±4	23±1	370±10	8.6±0.3
		J=4–3	21796±5	26±1	407±13	11±1
		J=2–1	21984±20	1.8±0.2	278±45	0.49±0.10
	HCO ⁺	J=3–2	21957±27	2.8±0.6	272±60	0.76±0.23
		J=4–3	—	—	—	—
		J=2–1	21976±16	2.8±0.3	341±47	0.96±0.16
	HNC	J=3–2	21954±23	4.0±0.5	302±54	1.2±0.3
		J=4–3	21879±34	6.0±1.8	235±84	1.4±0.7 ($<3\sigma$)
		J=2–1	22007±35	1.5±0.3	298±90	0.44±0.17 ($<3\sigma$)
		J=3–2	21955±71	1.3±0.5	469±138	0.62±0.30 ($<3\sigma$)
J=4–3	22057 (fix)	1.3±0.5	366 (fix)	0.49±0.19 ($<3\sigma$)		
IRAS 12127–1412 (2 kpc)	HCN	J=2–1	39967±32	2.1±0.3	463±80	0.94±0.21
		J=3–2	39958±13	2.7±0.1	524±32	1.3±0.1 ^A
		J=4–3	39907±44	2.0±0.3	602±98	1.2±0.2
	HCO ⁺	J=2–1	39937±35	2.1±0.3	474±93	0.95±0.23 ^A
		J=3–2	39979±15	2.3±0.2	454±31	0.97±0.09 ^A
		J=4–3	39953±65	1.4±0.3	614±186	0.81±0.30 ($<3\sigma$)
	HNC	J=2–1	39980±37	2.0±0.3	490±81	0.93±0.20 ^A
		J=3–2	39966±29	1.9±0.2	476±66	0.84±0.15 ^A
		J=4–3	40012±52	2.1±0.4	522±120	1.0±0.3
IRAS 13509+0442 (2 kpc)	HCN	J=2–1	40941±15	3.9±0.4	284±41	1.0±0.2
		J=3–2	40936±6	4.5±0.2	266±15	1.1±0.1
		J=4–3	40922±12	3.2±0.3	277±27	0.83±0.11
	HCO ⁺	J=2–1	40900±15	4.4±0.5	248±38	1.0±0.2
		J=3–2	40923±6	5.9±0.3	251±13	1.4±0.1
		J=4–3	40918±14	4.2±0.4	294±30	1.2±0.2
	HNC	J=2–1	40958±15	3.0±0.4	200±40	0.57±0.14
		J=3–2	40928±7	3.9±0.2	248±14	0.91±0.07
		J=4–3	40892±15	3.3±0.3	275±32	0.84±0.13
IRAS 15250+3609 (1.5 kpc)	HCN	J=2–1	16581±4	13±1	272±10	3.5±0.2
		J=3–2	16576±4	20±1	277±11	5.5±0.3
		J=4–3	16562±7	27±1	271±15	7.5±0.5
	HCO ⁺	J=2–1	16562±9	7.5±0.6	223±18	1.7±0.2
		J=3–2	16568±9	11±1	182±23	2.0±0.3
		J=4–3	16567±13	15±3	162±29	2.5±0.7
	HNC	J=2–1	16590±7	13±1	302±20	4.1±0.3
		J=3–2	16591±4	27±1	263±10	7.1±0.3
		J=4–3	16590±4	39±1	259±9	10±1
Superantennae (1 kpc)	HCN	J=2–1	18539±19	5.5±0.3	878±54	4.9±0.4

Table 9 continued on next page

Table 9 (*continued*)

Object	Molecule	Line	Gaussian fit			
			Velocity [km s ⁻¹]	Peak [mJy]	FWHM [km s ⁻¹]	Flux [Jy km s ⁻¹]
(1)	(2)	(3)	(4)	(5)	(6)	(7)
	HCO ⁺	J=3-2	18535±8	13±1	805±18	11±1
		J=4-3	18570±21	12±1	1166±62	14±1
		J=2-1	18505±21	4.3±0.3	665±52	2.9±0.3
		J=3-2	18546±10	11±1	774±23	8.2±0.3
	HNC	J=4-3	18534±23	8.3±0.5	741±57	6.1±0.6
		J=2-1	18504±22	2.9±0.2	661±57	1.9±0.2
		J=3-2	18506±26	2.5±0.2	672±59	1.7±0.2
		J=4-3	18503±57	2.7±0.5	640±129	1.7±0.5
IRAS 20551-4250 (1 kpc)	HCN	J=2-1	12890±1	23±1	202±2	4.8±0.1
		J=3-2	12892±1	35±1	191±3	6.8±0.1
		J=4-3	12891±1	54±1	175±3	9.6±0.2
	HCO ⁺	J=2-1	12887±1	34±1	214±3	7.4±0.1
		J=3-2	12887±1	53±1	198±2	11±1
		J=4-3	12882±1	78±1	184±3	15±1
	HNC	J=2-1	12892±2	12±1	182±5	2.3±0.1
		J=3-2	12894±2	22±1	164±4	3.7±0.1
IRAS 22491-1808 (1.5 kpc)	HCN	J=2-1	23320±6	13±1	435±14	5.5±0.2
		J=3-2	23313±6	19±1	457±14	8.4±0.3
		J=4-3	23307±7	30±1	481±18	14±1 ^C
	HCO ⁺	J=2-1	23286±8	8.6±0.3	456±19	3.8±0.2
		J=3-2	23293±15	9.3±0.6	463±40	4.2±0.4
		J=4-3	23309±10	17±1	576±23	9.4±0.5 ^C
	HNC	J=2-1	23318±10	10±1	356±24	3.6±0.3
		J=3-2	23299±5	23±1	376±14	8.6±0.4
IRAS 22491-1808 (1.5 kpc)		J=4-3	23301±5	26±1	361±15	9.2±0.5 ^C

^A Certain double-peaked emission signature is observed. We also attempted a double Gaussian fit, and found that its flux was 0–10% smaller than that of the single Gaussian fit. We adopt single Gaussian fit flux.

^B One emission and one absorption (dip near the emission center) components.

^C Revised value from that shown by [Imanishi & Nakanishi \(2014\)](#), after redefining the continuum flux level (§3).

NOTE— Col.(1): Object name. The adopted beam size in kpc is shown in parentheses. Col.(2): Molecule. Col.(2): Rotational J-transition line. Cols.(4)–(7): Gaussian fit of emission line in a 1–2 kpc beam spectrum at the continuum peak position. Col.(4): Optical local standard of rest (LSR) velocity (v_{opt}) of the emission line peak in km s⁻¹. Col.(5): Peak flux in mJy. Col.(6): Observed full width at half maximum (FWHM) in km s⁻¹. Col.(7): Gaussian-fit velocity-integrated flux in Jy km s⁻¹. Only the Gaussian fitting error (statistical uncertainty) is considered.

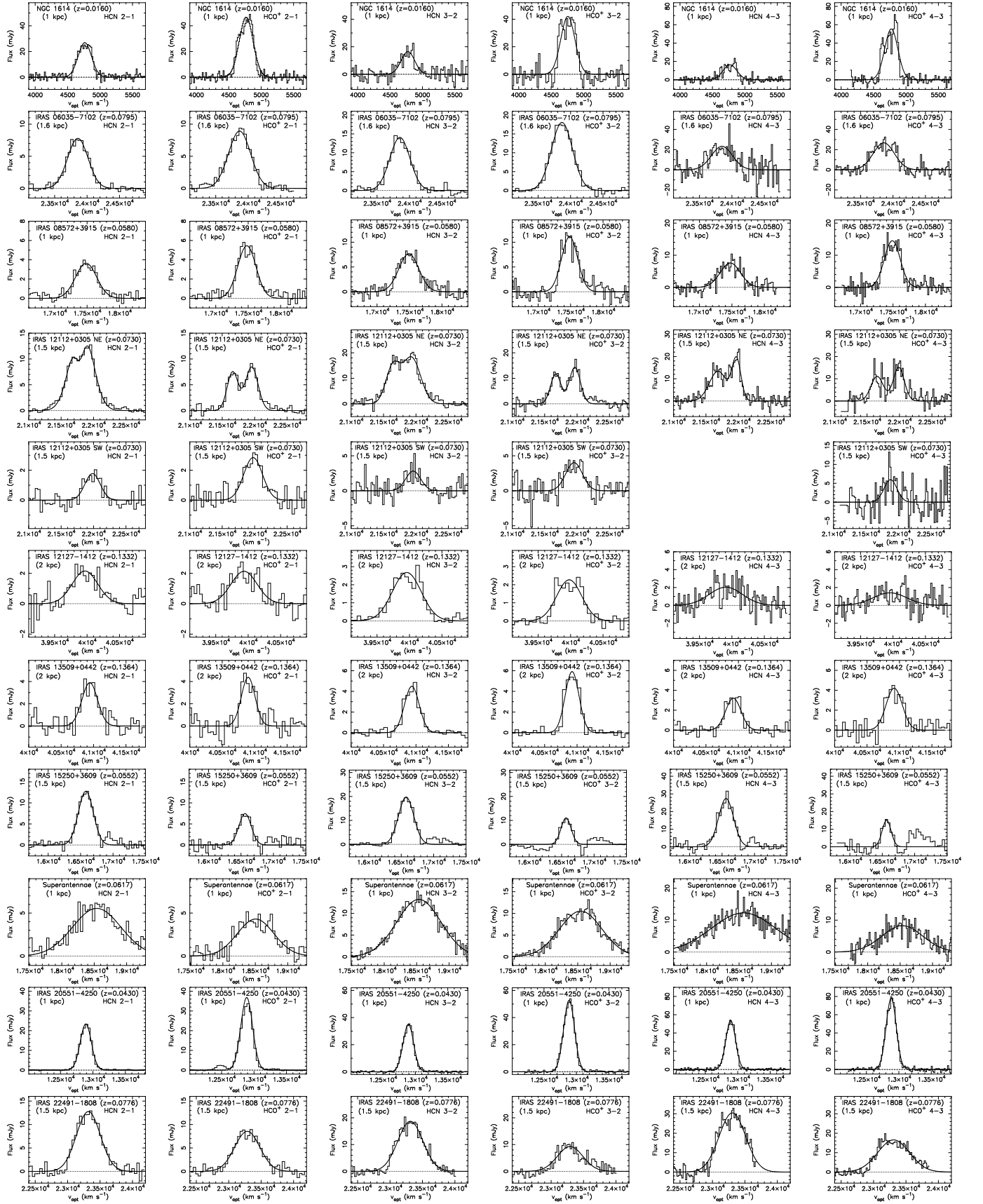


Figure 9. Adopted Gaussian fits (solid curved lines) of HCN and HCO⁺ emission lines. The abscissa is the optical LSR velocity in km s⁻¹ and the ordinate is the flux density in mJy. The horizontal black thin dotted straight line indicates the zero flux level. Fits for the J=2–1 lines of certain sources can be found in [Imanishi et al. \(2022\)](#), but are shown here again.

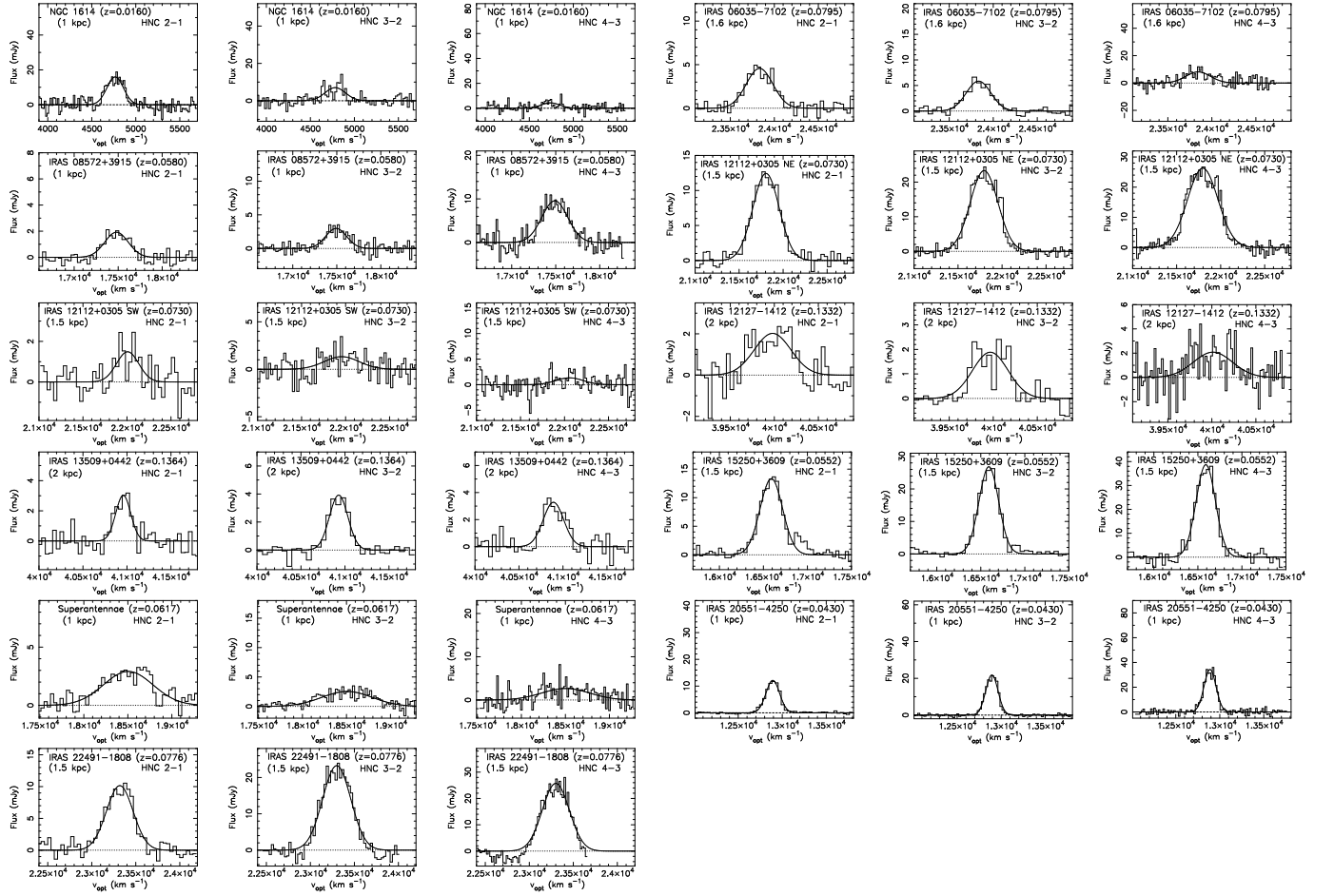


Figure 10. Adopted Gaussian fits (solid curved lines) of HNC emission line displayed in the same manner as Figure 9.

C. CONTINUUM FLUX DENSITY MEASURED WITH 1–2 KPC BEAM

Table 10 and Figure 11 show the continuum flux density and spectral energy distribution measured using the adopted 1–2 kpc beam, respectively. Using the continuum data, we attempted to make some correction of the possible absolute flux calibration uncertainty for individual ALMA observations (maximum $\sim 10\%$; §5.3) by assuming power law for an intrinsic continuum emission shape. However, in many (U)LIRGs, the observed continuum shape was concaved in such a way that 1.1–1.4 mm (band 6) flux was significantly smaller than the power law interpolation between 0.8–1.1 mm (band 7) and 1.4–1.8 mm (band 5) (e.g., clearly seen for IRAS 12127–1412, the Superantennae, and IRAS 20551–4250 in Figures 11f, 11i, and 11j). This is most likely because a dust thermal radiation component is significantly present in band 7 (0.8–1.1 mm) in addition to thermal free-free and synchrotron emission, which are dominant in bands 5 and 6 (1.1–1.8 mm). Thus, we decided not to apply this correction, because reliable correction turned out to be impossible.

Table 10. Continuum Emission in 1–2 kpc Beam

Object	Frequency	Flux	Peak Coordinate
	[GHz]	[mJy]	(RA,DEC)ICRS
(1)	(2)	(3)	(4)
NGC 1614 (1 kpc)	J21a; 181.2 (173.2–176.9, 185.4–189.1)	10 (7.5σ)	(04 34 00.0, –08 34 45)
	J21b; 185.4 (177.4–181.2, 189.6–193.3)	11 (5.1σ)	
	J32a; 263.2 (260.8–265.5)	12 (6.9σ)	
	J32b; 261.2 (251.8–255.5, 266.8–270.6)	12 (5.7σ)	
	J43a; 344.1 (336.2–338.0, 347.9–351.9)	22 (16σ)	
	J43b; 351.0 (344.1–346.0, 355.9–357.9)	16 (17σ)	
IRAS 06035–7102 (1.6 kpc)	J21a; 170.9 (163.1–166.7, 175.0–178.7)	1.1 (10σ)	(06 02 53.9, –71 03 10)
	J21b; 174.8 (166.9–170.7, 178.9–182.6)	1.2 (10σ)	
	J32a; 247.8 (245.4–250.2)	2.5 (18σ)	
	J32b; 245.9 (237.0–240.6, 251.0–254.7)	2.0 (24σ)	
	J43a; 323.4 (315.4–319.0, 327.4–331.3)	5.6 (5.2σ)	
	J43b; 342.9 (335.0–338.9, 347.1–350.7)	4.8 (4.4σ)	
IRAS 08572+3915 (1 kpc)	J21a; 168.1 (166.2–169.9)	1.8 (17σ)	(09 00 25.4, +39 03 54)
	J21b; 172.2 (170.3–174.1)	1.9 (17σ)	
	J32a; 252.7 (250.4–254.9)	3.0 (21σ)	
	J32b; 250.8 (241.8–245.4, 256.1–259.8)	2.0 (20σ)	
	J43a; 342.0 (334.2–337.9, 346.2–349.8)	6.1 (39σ)	
	J43b; 337.8 (329.9–333.6, 341.8–345.7)	6.7 (14σ)	
IRAS 12112+0305 NE (1.5 kpc)	J21a; 171.7 (163.9–167.5, 175.7–179.4)	3.5 (26σ)	(12 13 46.1, +02 48 42)
	J21b; 169.7 (167.9–171.5)	3.8 (16σ)	
	J32a; 249.1 (246.8–251.3)	9.0 (31σ)	
	J32b; 247.3 (238.3–242.0, 252.5–256.2)	8.4 (39σ)	
	J43a; 325.3 (317.3–321.0, 329.4–333.2)	17 (37σ)	
	J43b; 344.8 (336.9–340.8, 349.1–352.7)	13 (30σ)	
IRAS 12112+0305 SW (1.5 kpc)	J21a; 171.7 (163.9–167.5, 175.7–179.4)	0.39 (3.0σ)	(12 13 45.9, +02 48 39)

Table 10 continued on next page

Table 10 (*continued*)

Object	Frequency [GHz]	Flux [mJy]	Peak Coordinate (RA,DEC)ICRS
(1)	(2)	(3)	(4)
	J21b; 169.7 (167.9–171.5)	0.45 (1.9 σ)	
	J32a; 249.1 (246.8–251.3)	0.86 (3.0 σ)	
	J32b; 247.3 (238.3–242.0, 252.5–256.2)	1.0 (4.6 σ)	
	J43a; 325.3 (317.3–321.0, 329.4–333.2)	1.9 (3.9 σ)	
	J43b; 344.8 (336.9–340.8, 349.1–352.7)	1.9 (4.2 σ)	
IRAS 12127–1412 (2 kpc)	J21a; 150.8 (142.9–146.4, 155.1–158.7)	1.1 (16 σ)	(12 15 19.1, –14 29 42)
	J21b; 160.9 (159.0–162.7)	1.3 (20 σ)	
	J32a; 236.1 (233.7–238.4)	1.4 (25 σ)	
	J32b; 234.1 (225.5–229.0, 239.1–242.7)	1.5 (36 σ)	
	J43a; 307.9 (300.0–303.7, 312.0–315.8)	2.8 (21 σ)	
	J43b; 314.3 (307.6–309.5, 319.1–321.0)	2.6 (16 σ)	
IRAS 13509+0442 (2 kpc)	J21a; 150.4 (142.5–146.0, 154.7–158.2)	0.81 (11 σ)	(13 53 31.6, +04 28 05)
	J21b; 160.4 (158.5–162.2)	0.74 (9.4 σ)	
	J32a; 235.4 (233.1–237.7)	1.5 (20 σ)	
	J32b; 233.5 (224.9–228.4, 238.4–242.0)	1.5 (24 σ)	
	J43a; 307.1 (299.4–302.9, 311.1–314.8)	3.2 (23 σ)	
	J43b; 314.2 (306.4–309.9, 318.3–322.0)	3.7 (27 σ)	
IRAS 15250+3609 (1.5 kpc)	J21a; 168.5 (166.7–170.3)	5.7 (19 σ)	(15 26 59.4, +35 58 37)
	J21b; 172.7 (170.8–174.6)	7.0 (24 σ)	
	J32a; 253.4 (251.0–255.8)	11 (31 σ)	
	J32b; 251.5 (242.5–246.1, 256.7–260.5)	12 (35 σ)	
	J43a; 336.9 (334.9–338.8)	19 (22 σ)	
	J43b; 338.7 (330.8–334.4, 342.6–346.6)	24 (28 σ)	
Superantennae (1 kpc)	J21a; 167.5 (165.6–169.3)	3.9 (14 σ)	(19 31 21.4, –72 39 22)
	J21b; 171.6 (169.7–173.5)	4.3 (23 σ)	
	J32a; 252.0 (249.5–254.4)	5.3 (28 σ)	
	J32b; 250.0 (240.9–244.6, 255.3–259.0)	4.8 (34 σ)	
	J43a; 340.9 (333.0–336.8, 345.1–348.8)	9.5 (27 σ)	
	J43b; 336.7 (328.8–332.4, 340.7–344.5)	11 (37 σ)	
IRAS 20551–4250 (1 kpc)	J21a; 170.5 (168.6–172.3)	2.6 (45 σ)	(20 58 26.8, –42 39 00)
	J21b; 180.8 (172.8–176.5, 185.0–188.7)	2.8 (33 σ)	
	J32a; 254.2 (244.8–249.0, 259.8–263.5)	4.7 (29 σ)	
	J32b; 256.3 (254.0–258.5)	4.4 (38 σ)	
	J43a; 346.8 (338.9–342.8, 350.9–354.6)	12 (28 σ)	
	J43b; 341.6 (334.6–336.5, 346.7–348.6)	12 (26 σ)	
IRAS 22491–1808 (1.5 kpc)	J21a; 170.9 (163.2–166.8, 175.0–178.6)	2.3 (15 σ)	(22 51 49.4, –17 52 24)
	J21b; 169.1 (167.2–171.0)	2.9 (12 σ)	
	J32a; 248.4 (246.1–250.7)	4.8 (15 σ)	
	J32b; 246.6 (237.7–241.3, 251.8–255.5)	6.1 (30 σ)	
	J43a; 336.4 (328.5–332.3, 340.6–344.3)	11 (34 σ)	

Table 10 continued on next page

Table 10 (*continued*)

Object	Frequency	Flux	Peak Coordinate
	[GHz]	[mJy]	(RA,DEC)ICRS
(1)	(2)	(3)	(4)
J43b; 337.1 (336.1–338.0)		11 (31 σ)	

NOTE—Col.(1): Object name. The adopted beam size in kpc is shown in parentheses. Col.(2): Central frequency used for continuum extraction for J21a–J43b (explained in the caption of Table 2) in GHz is shown first, and the frequency range in GHz is listed in parentheses. The frequencies of obvious emission and absorption lines are removed. Col.(3): Continuum flux in mJy at the emission peak with adopted beam size. Value at the highest flux pixel ($0''.02$ – $0''.04$ pixel $^{-1}$) is extracted. Detection significance relative to root mean square (rms) noise is shown in parentheses. Possible systematic uncertainty arising from the absolute flux calibration ambiguity in individual ALMA observations and choice of the frequency range for continuum-level determination, are not included. Col.(4): Coordinate of continuum emission peak in ICRS.

For certain fractions of the observed ULIRGs, the photometric data at $250\ \mu\text{m}$, $350\ \mu\text{m}$, and $500\ \mu\text{m}$ taken with the Herschel Space Observatory are available (Clements et al. 2018). These data, together with the IRAS $60\ \mu\text{m}$ and $100\ \mu\text{m}$ fluxes, are usually dominated by dust thermal radiation, and are plotted in Figure 12. We overplot our ALMA continuum data measured with a 1–2 kpc beam in Figure 12. Our ALMA continuum fluxes largely agree with, or are only slightly smaller than, those extrapolated from shorter-wavelength IRAS and Herschel fluxes measured using larger beams ($\gtrsim 5''$ or $\gtrsim 5$ kpc at $z \gtrsim 0.05$). This rough agreement supports the previously argued scenario that nearby ULIRGs are energetically dominated by compact ($\lesssim 1$ – 2 kpc) nuclear regions (e.g., Soifer et al. 2000; Diaz-Santos et al. 2010; Imanishi et al. 2011; Pereira-Santaella et al. 2021), which are well covered with our ALMA data.

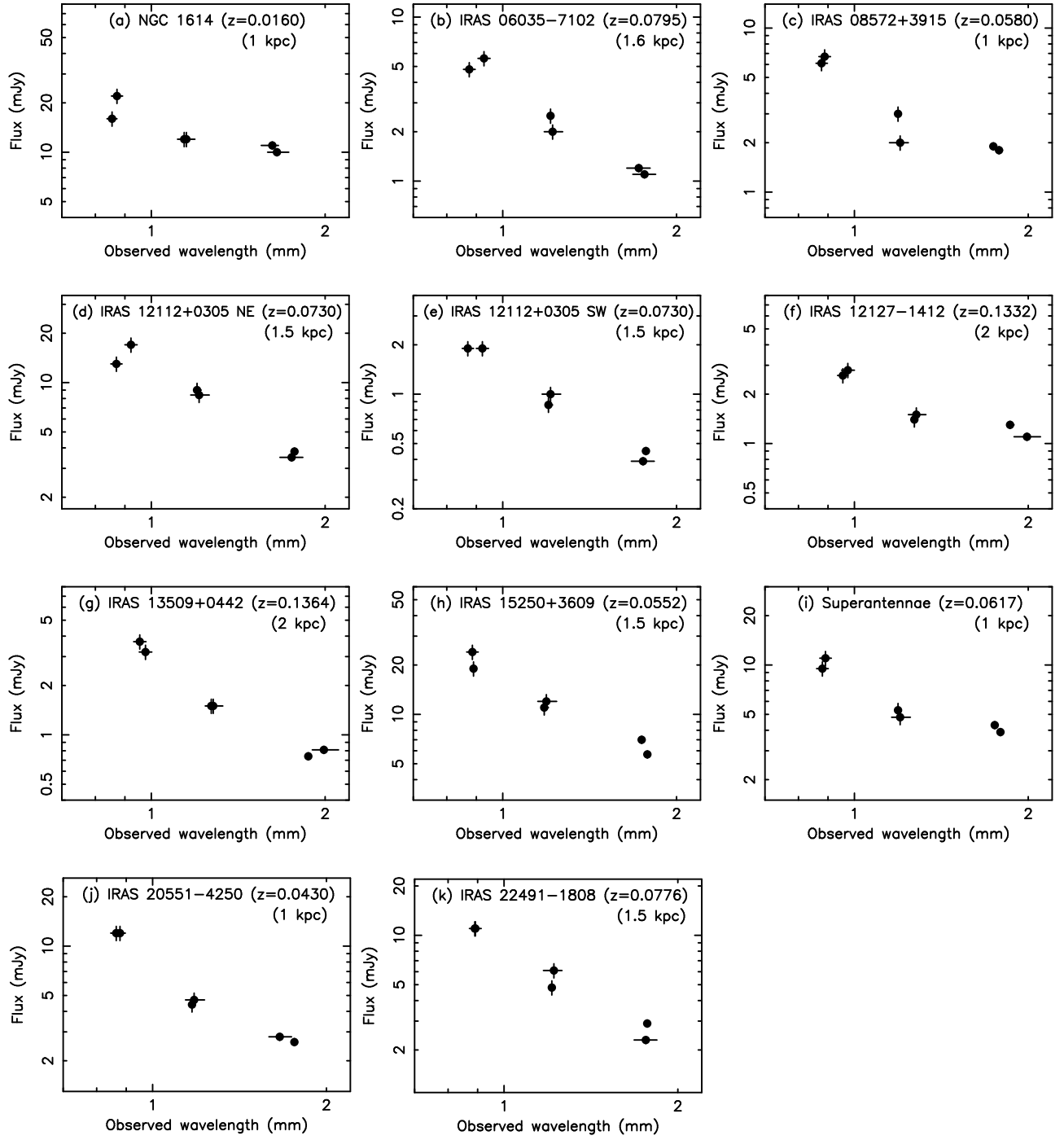


Figure 11. Continuum flux density in mJy (ordinate) as a function of observed wavelength in μm (abscissa) for the observed 11 (U)LIRGs' nuclei. 5–10% error is added in the ordinate, by considering the possible absolute flux calibration uncertainty of individual ALMA observations (§5.3). The object name, redshift, and adopted beam size in kpc are shown.

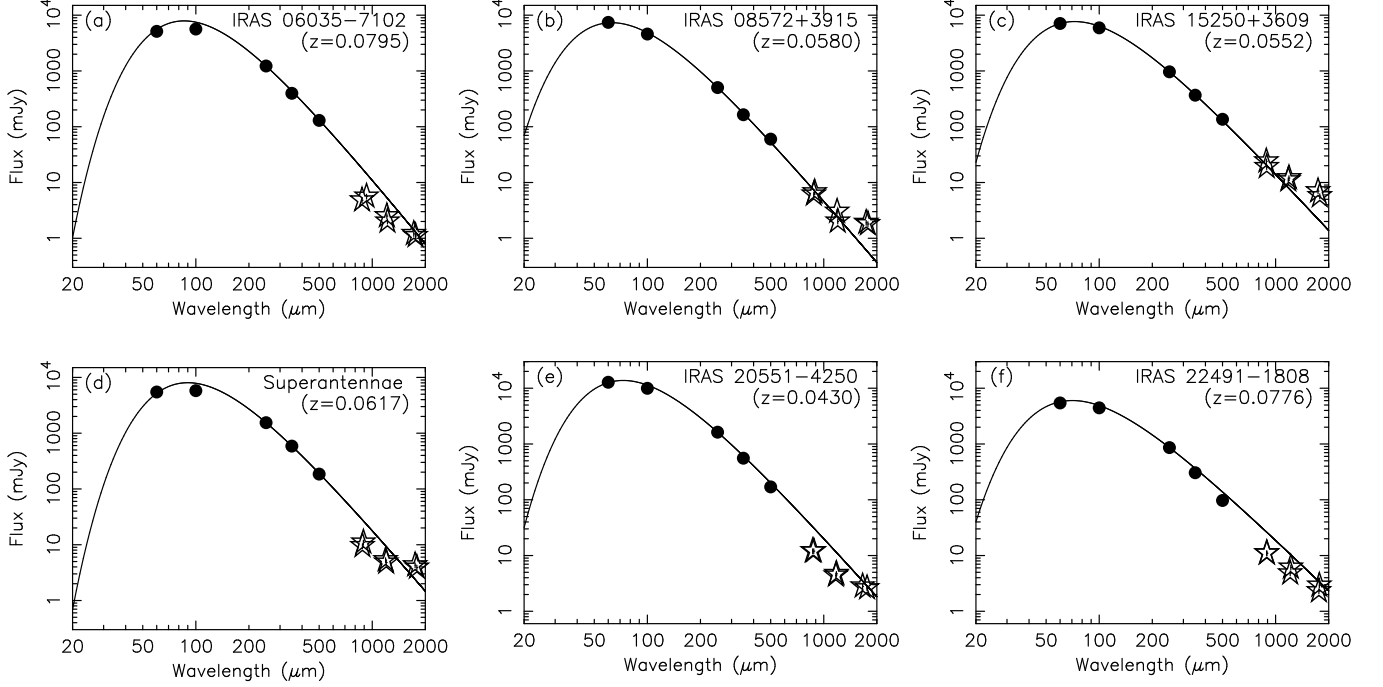
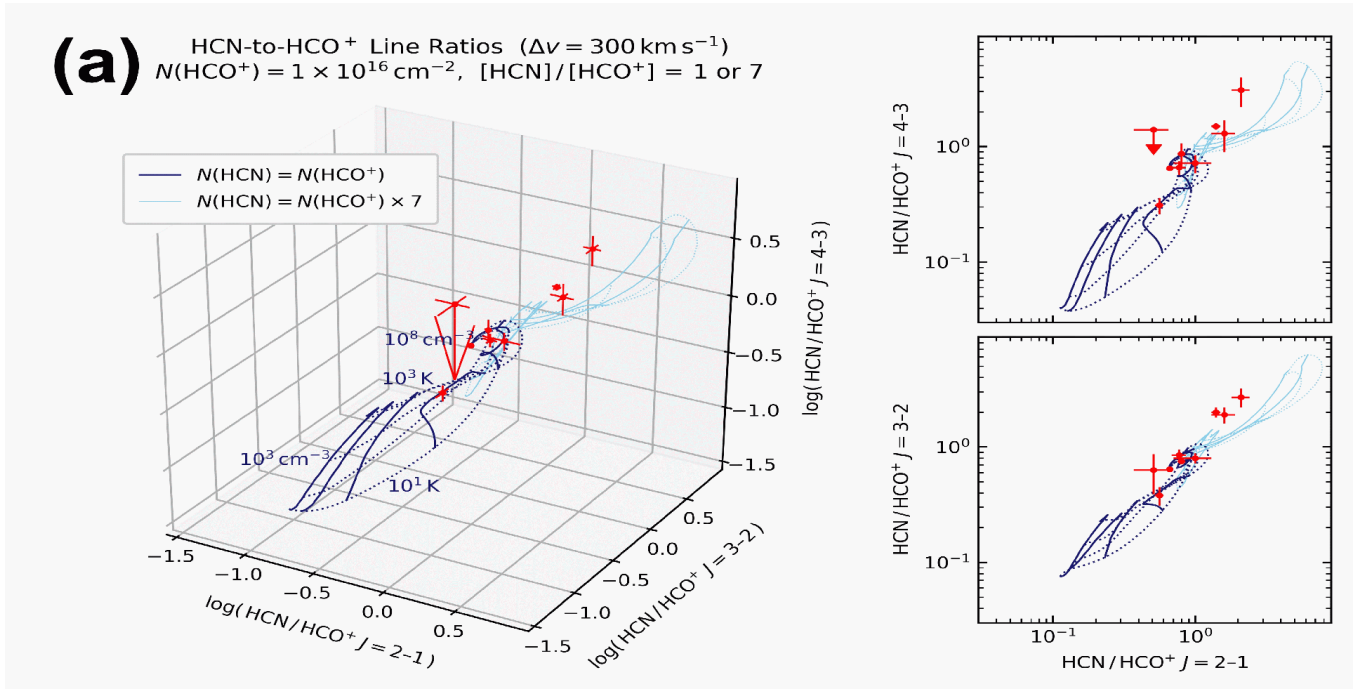


Figure 12. Continuum flux density in mJy (ordinate) as a function of observed wavelength in μm (abscissa) for selected ULIRGs, for which Herschel 250, 350, and 500 μm photometric data are available. Filled circle: Herschel photometric data (Clements et al. 2018). Open star: ALMA 1–2 kpc beam photometric data. The IRAS 60 μm and 100 μm fluxes are also plotted as filled circles. The thick curved lines represent the best-fit graybody curves adopted by Clements et al. (2018) after normalizing at the 250 μm flux.

D. COMPARISON OF OBSERVED HCN-TO-HCO⁺ FLUX RATIOS WITH RADEX MODELING USING DIFFERENT PARAMETERS

In Figure 13, the observed HCN-to-HCO⁺ flux ratios of (U)LIRGs' nuclei are compared with RADEX non-LTE modeling with significantly different values of HCN-to-HCO⁺ abundance ratio, HCO⁺ column density, and line width, from those adopted in §5.2. As evident, the overall distribution of the observed HCN-to-HCO⁺ flux ratios in the (U)LIRGs' nuclei are still better explained with an enhanced HCN-to-HCO⁺ abundance ratio, as argued in §5.2.



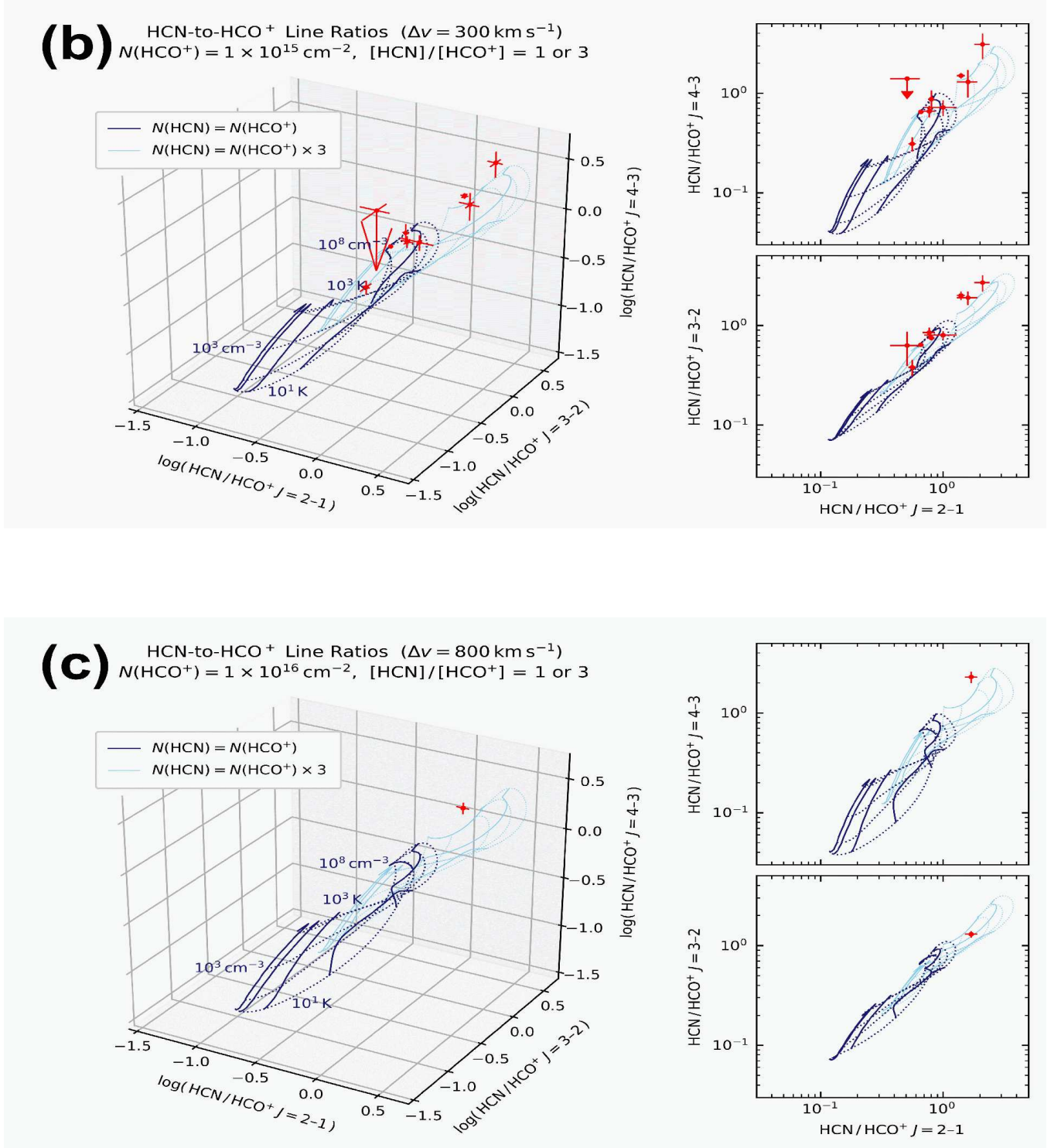


Figure 13. Same as Figure 3, but (a) for even higher HCN-to-HCO⁺ abundance ratio of $[\text{HCN}]/[\text{HCO}^+] = 7$, (b) for an order of magnitude smaller HCO⁺ column density of $N_{\text{HCO}^+} = 1 \times 10^{15} \text{ cm}^{-2}$, and (c) for a factor of ~ 2.3 larger line width of $\Delta v = 800 \text{ km s}^{-1}$. The red filled circles represent the observed HCN-to-HCO⁺ flux ratios of (a,b) the same (U)LIRGs' nuclei as plotted in Figure 3 and (c) the Superantennae which displays an exceptionally large line width compared to other (U)LIRGs' nuclei (Table 3, column 11).

REFERENCES

- Aalto, S., Garcia-Burillo, S., Muller, S., et al. 2015a, *A&A*, 574, A85
- Aalto, S., Martin, S., Costagliola, F., et al. 2015b, *A&A*, 584, A42
- Aladro, R., Martin, S., Riquelme, D., et al. 2015, *A&A*, 579, A101
- Armus, L., Charmandaris, V., Bernard-Salas, J., et al. 2007, *ApJ*, 656, 148
- Astropy Collaboration, Price-Whelan, A. M., Lim, P. L., et al. 2022, *ApJ*, 935, 167
- Baba, S., Nakagawa, T., Isobe, N., & Shirahata, M. 2018, *ApJ*, 852, 83
- Braitto, V., Reeves, J. N., Della Ceca, R., et al. 2009, *A&A*, 504, 53
- Bublitz, J., Kastner, J. H., Santander-Garcia, M., et al. 2019, *A&A*, 625, A101
- Butterworth, J., Holdship, J., Viti, S., & Garcia-Burillo, S., et al. 2022, *A&A*, 667, A131
- Byrd, R. H., Lu, P., Nosedal, J., & Zhu, C. 1995, *SIAM J. Sci. Comput.*, 16, 1190
- Clements, D. L., Pearson, C., Farrah, D., et al. 2018, *MNRAS*, 475, 2097
- Colina, L., Lipari, S., & Macchetto, F. 1991, *ApJ*, 379, 113
- Dartois, E., & Munoz-Caro, G. M. 2007, *A&A*, 476, 1235
- Diaz-Santos, T., Charmandaris, V., Armus, L., et al. 2010, *ApJ*, 723, 993
- Duc, P. -A., Mirabel, I. F., & Maza, J. 1997, *A&AS*, 124, 533
- Dudley, C. C., & Wynn-Williams, C. G. 1997, *ApJ*, 488, 720
- Farrah, D., Connolly, B., Connolly, N., et al. 2009, *ApJ*, 700, 396
- Foreman-Mackey, D. 2016, *The Journal of Open Source Software*, 1, 24
- Foreman-Mackey, D., Hogg, D. W., Lang, D., & Goodman, J., 2013, *PASP*, 125, 306
- Gao, Y., & Solomon, P. M. 2004, *ApJS*, 152, 63
- Garcia-Rodriguez, A., Usero, A., Leroy, A. K., et al. 2023, *A&A* in press (arXiv:2302.00450)
- Graninger, D. M., Herbst, E., Öberg, K. I., & Vasyunin, A. I. 2014, *ApJ*, 787, 74
- Greve, T. R., Papadopoulos, P. P., Gao, Y., & Radford, S. J. E. 2009, *ApJ*, 692, 1432
- Hailey-Dunsheath, S., Sturm, E., Fischer, J., et al. 2012, *ApJ*, 755, 57
- Harris, C. R., Millman, K. J., van der Walt, S., et al. 2020, *Nature*, 585, 357
- Hildebrand, R. H. 1983, *QJRAS*, 24, 267
- Hirota, T., Yamamoto, S., Mikami, H., & Ohishi, M. 1998, *ApJ*, 503, 717
- Hunter, J. D. 2007, *Computing in Science and Engineering*, 9, 90
- Imanishi, M., & Dudley, C. C. 2000, *ApJ*, 545, 701
- Imanishi, M., Dudley, C. C., Maiolino, R., et al. 2007, *ApJS*, 171, 72
- Imanishi, M., Dudley, C. C., & Maloney, P. R. 2006, *ApJ*, 637, 114
- Imanishi, M., Hagiwara, Y., Horiuchi, S., Izumi, T., & Nakanishi, K. 2021, *MNRAS*, 502, L79
- Imanishi, M., Imase, K., Oi, N., & Ichikawa, K. 2011, *AJ*, 141, 156
- Imanishi, M., Nakagawa, T., Ohyama, Y., et al. 2008, *PASJ*, 60, S489
- Imanishi, M., Nakagawa, T., Shirahata, M., Ohyama, Y., & Onaka, T. 2010, *ApJ*, 721, 1233
- Imanishi, M., & Nakanishi, K. 2013a, *AJ*, 146, 47
- Imanishi, M., & Nakanishi, K. 2013b, *AJ*, 146, 91
- Imanishi, M., & Nakanishi, K. 2014, *AJ*, 148, 9
- Imanishi, M., Nakanishi, K., & Izumi, T. 2016a, *ApJ*, 825, 44
- Imanishi, M., Nakanishi, K., & Izumi, T. 2016b, *AJ*, 152, 218
- Imanishi, M., Nakanishi, K., & Izumi, T. 2018, *ApJ*, 856, 143
- Imanishi, M., Nakanishi, K., & Izumi, T. 2019, *ApJS*, 241, 19
- Imanishi, M., Nakanishi, K., Izumi, T., & Baba, S. 2022, *ApJ*, 926, 159
- Imanishi, M., Nguyen, D. D., Wada, K., et al. 2020, *ApJ*, 902, 99
- Israel, F. P. 2022, *A&A*, in press (arXiv:2212.00814)
- Izumi, T., Kawakatu, N., & Kohno, K. 2016b, *ApJ*, 827, 81
- Izumi, T., Kohno, K., Aalto, S., et al. 2016a, *ApJ*, 818, 42
- Juneau, S., Narayanan, D. T., Moustakas, J., et al. 2009, *ApJ*, 707, 1217
- Kamenno, S., Sawada-Satoh, S., Impellizzeri, C. M. V., et al. 2020, *ApJ*, 895, 73
- Kewley, L. J., Heisler, C. A., Dopita, M. A., & Lumsden, S. 2001, *ApJS*, 132, 37
- Kim, D. -C., & Sanders, D. B. 1998, *ApJS*, 119, 41

- Kluyver, T., Ragan-Kelley, B., Perez, F., et al. 2016, in *Positioning and Power in Academic Publishing: Players, Agents and Agendas* (IOS Press), 87–90
- Krips, M., Neri, R., Garcia-Burillo, S., et al. 2008, *ApJ*, 677, 262
- Leroy, A. K., Usero, A., Schrubba, A., et al. 2017, *ApJ*, 835, 217
- Leroy, A. K., Rosolowsky, E., Usero, A., et al. 2022, *ApJ*, 927, 149
- Lu, N., Zhao, Y., Diaz-Santos, T., et al. 2017, *ApJS*, 230, 1
- Manohar, S., & Scoville, N. 2017, *ApJ*, 835, 127
- Martin, S., Aalto, S., Sakamoto, K., et al. 2016, *A&A*, 590, A25
- Martin, S., Mauersberger, R., Martin-Pintado, J., et al. 2006, *ApJS*, 164, 450
- Mashian, N., Sturm, E., Sternberg, A., et al. 2015, *ApJ*, 802, 81
- Meijerink, R., Kristensen, L. E., Weiss, A., et al. 2013, *ApJ*, 762, L16
- Meijerink, R., Spaans, M., & Israel, F. P. 2007, *A&A*, 461, 793
- Mirabel, I. F., Lutz, D., & Maza, J. 1991, *A&A*, 243, 367
- Moreno, J., Torrey, P., Ellison, S., et al. 2019, *MNRAS*, 485, 1320
- Nakajima, T., Takano, S., Kohno, K., Harada, N., & Herbst, E. 2018, *PASJ*, 70, 7
- Nardini, E., Risaliti, G., Watabe, Y., Salvati, M., & Sani, E. 2010, *MNRAS*, 405, 2505
- Newville, M., Otten, R., Nelson, A., et al. 2021, *lmfit/lmfit-py: 1.0.3*, Zenodo, Zenodo
- Papadopoulos, P. P., van der Werf, P., Xilouris, E., et al. 2012a, *ApJ*, 751, 10
- Papadopoulos, P. P., van der Werf, P. P., Xilouris, E. M., et al. 2012b, *MNRAS*, 426, 2601
- Papadopoulos, P. P., Zhang, Z.-Y., Xilouris, E. M., et al. 2014, *ApJ*, 788, 153
- Pereira-Santaella, M., Colina, L., Alonso-Herrero, A., et al. 2015, *MNRAS*, 454, 367
- Pereira-Santaella, M., Colina, L., Garcia-Burillo, S., et al. 2021, *A&A*, 651, A42
- Pereira-Santaella, M., Spinoglio, L., van der Werf, P. P., et al. 2014, *A&A*, 566, A49
- Perez, F., & Granger, B. E. 2007, *Computing in Science and Engineering*, 9, 21
- Reback, J., jbrockmendel, McKinney, W., et al. 2022, *pandas-dev/pandas: Pandas 1.4.2, v1.4.2*, Zenodo, Zenodo
- Risaliti, G., Maiolino, R., Marconi, A., et al. 2003, *ApJ*, 595, L17
- Risaliti, G., Maiolino, R., Marconi, A., et al. 2006, *MNRAS*, 365, 303
- Rosenberg, M. J. F., van der Werf, P. P., Aalto, S., et al. 2015, *ApJ*, 801, 72
- Saito, T., Iono, D., Ueda, J., et al. 2018, *MNRAS*, 475, L52
- Sakamoto, K., Martin, S., Wilner, D. J., et al. 2021, *ApJ*, 923, 240
- Sanders, D. B., Mazzarella, J. M., Kim, D. -C., Surace, J. A., & Soifer, B. T. 2003, *ApJ*, 126, 1607
- Sanders, D. B., & Mirabel, I. F. 1996, *ARA&A*, 34, 749
- Sani, E., Risaliti, G., Salvati, M., et al. 2008, *ApJ*, 675, 96
- Schilke, P., Walmsley, C. M., Pineau des Forets, G., et al. 1992, *A&A*, 256, 595
- Scoville, N., Sheth, K., Walter, F., et al. 2015, *ApJ*, 800, 70
- Shirley, Y. L. 2015, *PASP*, 127, 299
- Sliwa, K., & Downes, D. 2017, *A&A*, 604, A2
- Soifer, B. T., Neugebauer, G., Matthews, K., et al. 2000, *AJ*, 119, 509
- Spaans, M., & Meijerink, R. 2008, *ApJ*, 678, L5
- Spoon, H. W. W., Keane, J. V., Tielens, A. G. G. M., Lutz, D., Moorwood, A. F. M., & Laurent, O. 2002, *A&A*, 385, 1022
- Spoon, H. W. W., Tielens, A. G. G. M., Armus, L., et al. 2006, *ApJ*, 638, 759
- Stierwalt, S., Armus, L., & Surace, J. A., et al. 2013, *ApJS*, 206, 1
- Takano, S., Nakajima, T., & Kohno, K. 2019, *PASJ*, 71, S20
- THE CASA Team, Bean, B., Bhatnagar, S., et al. 2022, *PASP*, 134, 114501
- Tunnard, R., Greve, T. R., Garcia-Burillo, S., et al. 2015, *ApJ*, 800, 25
- Ueda, J., Iono, D., Yun, M. S., et al. 2021, *ApJS*, 257, 57
- van der Tak, F. F. S., Black, J. H., Schoier, F. L., Jansen, D. J., & van Dishoeck, E. F. 2007, *A&A*, 468, 627
- Veilleux, S., Kim, D. -C., & Sanders, D. B. 1999, *ApJ*, 522, 113
- Veilleux, S., Kim, D. -C., Sanders, D. B., Mazzarella, J. M., & Soifer, B. T. 1995, *ApJS*, 98, 171

- Veilleux, S., Rupke, D. S. N., Kim, D.-C., et al. 2009, *ApJS*, 182, 628
- Virtanen, P., Gommers, R., Oliphant, T. E., 2020, *Nature Methods*, 17, 261
- Viti, S., Garcia-Burillo, S., Fuente, A., et al. 2014, *A&A*, 570, A28
- Yamada, M., Wada, K., & Tomisaka, K. 2007, *ApJ*, 671, 73
- Yuan, T. -T., Kewley, L. J., Sanders, D. B. 2010, *ApJ*, 709, 884